Development of Electric-Driven Cryogenic Pump for Upper Stage Hybrid Rockets

by

Kaan Gegeoğlu

A Dissertation Submitted to the
Graduate School of Sciences and Engineering
in Partial Fulfillment of the Requirements for
the Degree of

Master of Science

in

Mechanical Engineering

KOÇ UNIVERSITY

April 2020

Development of Electric-Driven Cryogenic Pump for Upper Stage Hybrid Rockets

Koç University

Graduate School of Sciences and Engineering

This is to certify that I have examined this copy of a master's thesis by

Kaan Gegeoğlu

and have found that it is complete and satisfactory in all respects,
and that any and all revisions required by the final
examining committee have been made.

Committee Members:

____
Assoc. Prof. Arif Karabeyoğlu (Advisor)

____
Assoc. Prof. Çağlar Üçler

____
Prof. İsmail Lazoğlu

Date: ______________________

This thesis is dedicated to my beloved family, my dear girlfriend, Elif, and my dear friends who supported me throughout this journey as well as my thesis advisor Assoc. Prof. Arif Karabeyoglu, who has been a source of inspiration for me before, during and after the study.

ABSTRACT

The performance of a rocket propulsion system utilizing liquid propellants depends on the propellant feed system (PFS) performance and capability. A PFS must be able to deliver the propellant at the desired flow rate and pressure into the combustion chamber.

The most commonly used mechanisms for PFS consist of pressurization by a cold gas or pressurization by a pump. The first method requires pressurizing the entire feed system including propellant tanks to its delivery pressure while the second one pressurizes only a small portion of the feed line but requires a mechanical power source. These two methods have been used widely where pumps are employed on high thrust and power applications while cold gas pressurization is employed on relatively small and less sophisticated systems. The reason for this is that only capable power sources for high-performance pumps were turbines and this approach was not viable for lower thrust level systems due to its complexity and cost. As the space industry leans towards micro-satellites, the development of launch vehicles in this class is gaining more attention. Weight disadvantage of pressure-fed systems, complexity, development cost and time of turbopump systems and emerging power electronics, battery, and electric motor technologies arouse the question of the viability of electric driven pumps on micro-satellite level propulsion systems.

This study is aimed to show the advantages of electric pump utilization over cold gas pressurization in hybrid rockets through an electric pump development process. For this, a hydraulic and mechanical design is made from a set of system requirements and the performance of this pump is assessed by means of CFD analysis. The CFD model is validated by pump tests. Then two separate hybrid rocket propulsion systems are designed, one of which employs electric pump and the other is pressure-fed. A system-level comparison of performance on different operational parameters, concluding high fidelity evidence for the thesis argument. Final results show that electric pumps are quite beneficial for upper stage hybrid rocket propulsion systems.

ÖZETÇE

Yanıcı veya yakıcı maddelerinden en az birini sıvı fazda barındıran bir roket itki sisteminin performansı, yakıt besleme sistemi performansına bağlıdır. Yakıt besleme sistemi, sıvı fazdaki yakıtı istenen basınç ve debi değerlerinde yanma odasına iletmelidir.

Yakıt besleme sistemi, basınçlandırma mekanizması olarak yüksek basınçlı soğuk gaz veya pompa kullanır. İlk metot, yakıt tankları da dahil olmak üzere tüm besleme sistemini enjektör basıncına getirmeyi gerektirir. İkincisi ise besleme sisteminin küçük bir kısmını enjektör basıncına getirse de pompayı sürmek için bir mekanik güç kaynağı gerektirmektedir. Yüksek itki ve güç gereksinimi olan sistemlerde pompa sistemi kullanılırken göreceli olarak düşük itkili ve daha az karmaşık sistemlerde soğuk gaz basınçlandırması kullanılmaktadır. Bunun sebebi, şimdiye kadar sadece türbin sistemlerinin yüksek performanslı pompaları sürmek için yetkin sistemler olması ve bunun karmaşıklık ve maliyet bakımından düşük itki sistemleri için uygun bulunmaması olmuştur. Uzay sektörünün mikro uydu uygulamalarına yönelmesi, bu uyduları fırlatacak daha düşük itki seviyeli fırlatma araçlarının geliştir-mesinin daha fazla ilgi görmesine neden olmaktadır. Soğuk gaz basınçlandırma sistemlerinin ağırlık dezavantajı, turbopompaların karmaşıklığı, geliştirme süresi ve maliyeti, ve güç elektronikleri, pil ve elektrik motoru teknolojilerindeki gelişmeler, elektrikli pompa sistemlerinin uygunluğu hakkındaki soruları gündeme getirmiştir.

Bu tezin amacı, üst kademe karma roketlerde elektrikli pompa tasarımı ve geliştirmesi yolu ile tasarlanan sistemin, soğuk gaz basınçlandırması yöntemine göre avantajlarını göstermektir. Bunun için sistem gereksinimlerinden yola çıkarak bir pompanın hidrolik ve mekanik tasarımı yapılmış ve pompanın performansı hesaplamalı akışkanlar dinamiği analizleri ile irdelenmiştir. Hesaplamalı akışkanlar dinamiği modeli gerçek bir sistem üzerinde test yöntemi ile doğrulanmıştır. Sonrasında, biri elektrikli pompa kullanan diğeri ise soğuk gaz basınçlandırması kullanan iki ayrı karma roket itki sistemi tasarlanmıştır. Sistem seviyesinde bu iki sistemin perfor-

mansı farklı operasyonel parametreler düzeyinde incelenmiş ve bu tezin argümanına destekleyici bir kanıt olarak sonuçlar sunulmuştur. Bu tezin sonucunda, elektrikli pompaların üst kademe karma roket itki sistemleri için oldukça faydalı bir çözüm olduğu belirtilmiştir.

ACKNOWLEDGMENTS

For helping me completing this study, I would like to thank to my advisor Arif Karabeyoglu for giving me his support though out the study; DeltaV Uzay Teknolojileri A.S. for providing me necessary tools and components, utilizing its test facility for this project and providing support in manufacturing. I also wish to extend my special thanks to my colleagues who helped me in this project where needed help, especially to Murat Cetinkaya and Sule Ozturk who showed interest and offered help for this study; Caglar Ucler for providing technical consultancy at DeltaV; Caglar Ozturk for instructing about pump CFD procedures and Habas personnel Aydin Seckin for providing technical support about the industrial pump that has been acquired for CFD validation purposes.

TABLE OF CONTENTS

LIST OF TABLES

LIST OF FIGURES

NOMENCLATURE

A	Area
a	Regression Rate Coefficient, Volute Throat Height
AR	Nozzle Area Ratio
b	Blade Width
c	Flow Velocity (Inside the Pump)
C_d	Discharge Coefficient
C_F	Thrust Coefficient
c^*	Characteristic Velocity
D	Diameter
e	Blade Thickness
G	Mass Flux
g_0	Acceleration of Earth's Gravity
H	Head
h	Specific Enthalpy
I_{sp}	Specific Impulse
K	Velocity Coefficient, Stress Concentration Factor
k	Turbulent Kinetic Energy
k_s	Safety Factor
L	Length
M, m	Mass
N	Rotational Speed (rpm)
N_s	Specific Speed $(\mathrm{gpm}, \mathrm{ft}, \mathrm{rpm})$
n	Regression Rate Exponent, Polytropic Coefficient
n_q	Specific Speed $(\mathrm{m^3/s}, \mathrm{m}, \mathrm{rpm})$
n_s	Specific Speed $(\mathrm{m^3/s}, \mathrm{m}, \mathrm{rad/s})$
$NPSH$	Net Positive Suction Head
O/F	Oxidizer to Fuel Mass Ratio

P, p	Pressure, Power
R	Specific Gas Constant
S	Surface Area
r	Radius
Q	Volumetric Flow Rate
T	Thrust, Torque, Temperature
t	Time
U	U
u	Tangential velocity component, Specific Energy
V	Velocity, Volume
v	Specific Volume
w	Relative Flow Velocity (Inside the Pump)
x	Space Variable
Z	Number of Blades
α	Angle with axial direction
β	Angle with tangential direction
γ	Slip Factor, Ratio of Specific Heats
δ	Mass Specific Power
ϵ	Solidity, Turbulent Dissipation Rate
η	Efficiency
λ	Blade Twist Angle
μ	Dynamic Viscosity
ρ	Density
σ	Cavitation coefficient
σ_y	Yield Stress
τ	Blade Blockage Factor
ϕ	Flow Coefficent
Ψ	Head Coefficient
ω, Ω	Angular Speed (rad/s)

Subscripts

1	Impeller/Blade Inlet
2	Impeller/Blade Outlet
3	Volute Outlet
B	Blade
a	Ambient
ab	Nozzle Ablative Layer
b	Burn
bat	Battery
bo	Burn out
ch	Combustion
dry	Without propellant or pressurization gas
del	Delivered
E	Energy Related
e	Exit
eff	Effective
em	Electric Motor
ESC	Electronic Speed Controller
f	Final
$fuel$	Fuel
h	Hydraulic
i	Ideal, Input, Initial
inj	Injector
j	Nozzle Jacket
m	Meridional component
$nozzle$	Nozzle
opt	Optimal
ox	Oxidizer
$oxtank$	Oxidizer Tank

P	Power
p	Fuel Port
pay	Payload
pg	Pressurization Gas
$pressfed$	Pressure-fed
$presstank$	Pressurization Tank
$prop$	Propellant
$pump$	Pump
$pumpfed$	Electric Pump-fed
ref	Reference
req	Required
s	Specific, Isentropic
ss	Suction Specific
st	Static
$stage$	Stage
sys	System
t	Turbulent
tot	Total
u	Tangential component
v	Vapor
x	x% Head Loss
Supercripts	
'	Actual
*	Nozzle Throat
e	Exit
t	At timestep t

Abbreviations

AISI	American Iron And Steel Institute
CAD	Computer Aided Design
CEE	Cylindrical with ellipsoidal ends
CFD	Computational Fluid Dynamics
CHE	Cylindrical with hemispherical ends
DAQ	Data Acquisition
LEO	Low Earth Orbit
LOX	Liquid Oxygen
MMH	Mono-Methyl Hydrazine
NTO	Nitrogen Tetroxide
PFS	Propellant Feed System
PMSM	Permanent Magnet Synchronous Motor

Chapter 1

INTRODUCTION

Sending objects into the earth's orbits requires working against gravity. This is achieved until today with rockets. Rockets produce thrust by expelling molecules that are energized and accelerated through a nozzle. Rockets differ by ways of putting energy into those molecules called propellants. This can be done by accelerating particles by an electric field, heating particles by nuclear energy or heating particles by exothermic chemical reactions. Energy added to particles is converted into kinetic energy by nozzles. Produced thrust by this process can simply be written out in the following form.

$$T = M\dot{V} = \dot{m}V_e \tag{1.1}$$

Where T is the thrust force and M is the mass of the vehicle $\dot{V}$ is the acceleration of that vehicle. Thrust is also equal to the product of the mass flow rate denoted by $\dot{m}$ with exhaust velocity V_e.

When launching to an orbit from the surface of the earth, depending on the size and weight of the vehicle to be launched, thrust requirements vary on a large scale. That means the product of the rate of mass expelled from the nozzle and the velocity attained by energy addition should meet the thrust requirements. In that regard, chemical rockets have been preferred over other types of propulsion although the exit velocity attained per particle (characteristic velocity) is lower than the electric or nuclear type of propulsion. The reason is that the amount of propellant expelled in unit time can be easily scaled up in chemical rocket propulsion.

Chemical rockets also divided into subgroups by choice of propellant combinations. Solid rockets have their propellants in premixed solid phase while liquid rockets carry their propellants in liquid phase inside the tanks on board. Hybrid rockets, on the other hand, uses the advantage of solid propellants by their low technological cost and convenience of use in solid phase, usually fuel, and benefits the advantage of throttling, shut-off and restart abilities by carrying the other propellant, usually the oxidizer, in liquid phase.

Chemical energy obtained from the combustion reaction depends strongly on the selection and initial properties of the propellants. Molecular weight also plays a very important role since the exhaust velocity inversely proportional to the molecular weight of the combustion products. Propellant selection is made due to current technologies and operational preferences therefore exhaust velocity can vary between different types of rockets. Nevertheless, the mass flow rate through the nozzle can be adjusted to obtain the required thrust.

To adjust the mass flow rate for a solid rocket, either the physical dimension of the grain such as port area or, burning rate (regression rate) should be modified. Solid propellants' burning rate is usually not a problem since it is on a sufficient level at the current technology level and the propellant flow rate can easily be adjusted by scaling the grain. However, if geometric envelope and port shape are constrained, achieving a high mass flow rate is only possible by higher combustion pressures since the burning rate is strongly dependent on the pressure. This has an adverse effect on the weight of the vehicle since combustion chamber walls have to be thick enough to withhold such pressure. In liquid and hybrid rockets, the mass flow rate is set by injection of liquid propellant into the combustion chamber through injectors. To achieve the desired fluid flow rate in injectors, a differential pressure must be established between the upstream and downstream of the injector. The mass flow rate is a function of the density of the fluid, injector area and the pressure difference across.

$$\dot{m}_{ox} = f(\rho_{ox}, A_{inj}, p_{inj}, p_{ch}) \tag{1.2}$$

This physical relation inherently requires pressurizing the liquid propellant to a higher pressure than there is at the combustion chamber. This pressurization process is achieved by different techniques.

One method that is applied in the early stage of liquid rockets is pressurizing the propellant tanks with high-pressure cold gas. This method is called cold gas pressurization system(or pressure fed system) and it is still used in small to medium scale propulsion systems. The advantage of such a system is the low development cost and time. Despite the advantages of the system, there is substantial performance loss, except for propulsion systems with small total impulse, due to additional weight in high-pressure tanks and pressurization gas that are carried on board. Operational hazards are also present due to high pressures on systems where technical personnel are near the vehicle before launch. For most systems, hazard is a secondary issue since there is always some high pressure gas somewhere for a launch vehicle, but potential for leak for a light gas like He at high pressures is important.

The other method to pressurize the propellant is doing mechanical work on the fluid to convert this mechanical energy to pressure. This is done by pumps that convert mechanical work into hydraulic work that increases pressure. For large flow rates, a centrifugal type pump that uses a fast spinning impeller to pressurize the fluid are used. A source of mechanical power is needed to drive pumps. In the history of rocket turbo-pumps, pump drive has been handled by a turbine [Sutton and Biblarz, 2010]. Turbines are driven by high-pressure gas generated by a gas generator, expander-cycle or by combustion chamber pressure with a tap-off method. An alternative solution for obtaining shaft power is an electric motor. This method is not used extensively in the history of rocketry due to the technological level of the electrical components at the time. Low power density of the motors and inadequate performance of batteries, lead scientists and engineers to focus more on the turbine technology.

With the recent advancements in electric motors, power electronics, and battery technologies, this approach became more and more promising to be applied to space systems. Electric motors are now capable of delivering more power and torque with reduced weight and dimensions, batteries' power and energy density are substantially increased with state-of-the-art battery technologies and power electronics control motor speed and torque with enhanced efficiencies.

Driving pumps with electric motors has various advantages over turbopump systems. Developing a new propellant feed system with turbopumps, requires extensive development for turbines, expensive manufacturing processes to produce turbines and long development times. Additionally, if a cryogenic fluid is being pumped, a single shaft needs to perform on extremely high and extremely low temperatures in both ends or a gear system needs to be employed that adds additional weight.

Electric pump systems, on the other hand, are much simple to design in a fast and safe manner due to the lack of need to manage another combustion device with its own propellant management.

Since these technological advancements in electric motor and batteries were presented, scientists and engineers have begun to assess the advantage of such an approach on propellant feed systems. There has been significant research suggesting the viability and comparative advantage of electric pump-fed systems.

Initial research about electric pump-fed systems focused on liquid rocket applications. Solda and Lentini [Solda and Lentini, 2008] assessed the feed system mass of a liquid propulsion system over various burn time and combustion chamber pressure, and showed the advantage of an electric pump-fed system especially with longer burn time and higher chamber pressures. In a later analysis, Rachov et. al. proposed "a remarkable extension of the possible field of application" of electric pumps compared to the previous work mentioned [Rachov et al., 2013].

Another comparison is made by Kwak et. al. with a gas generator cycle, and system weight analysis made for the application of both systems on KLSV-II 3rd stage. The authors drew attention to the simplicity of the "elec-pump" system in terms of development and ignition sequence. They reported a specific impulse gain due to lack of gas generator that expels propellant while generating any significant thrust. They also found a slight decrease in payload capability when employed electric pump cycle for given conditions but the advantage of the electric pump cycle is still evident for higher combustion chamber pressures in the study [Kwak et al., 2018].

Moving to small satellite launchers, Waxenegger-Wilfing et. al. presented the application of electric motors for propellant pumps of micro-launchers. They have developed a genetic algorithm to optimize stages for various payload configurations. Results show electric pump cycle optimizes towards lower chamber pressure due to power requirements although lower chamber pressures result in lower Isp in liquid rocket engines [Waxenegger-Wilfing et al., 2018].

Apart from the research, RocketLab developed an operational electric pump-fed system and implemented the approach to its Rutherford engine[1] . And it is the first

[1]Accessed on 25.02.2020,URL : https://www.spacelaunchreport.com/electron.html .

and only electric pump-fed rocket which has a flight-heritage so far.

As a summary, the liquid rocket community acknowledged and investigated the electric pump-fed concept for their convenient applications. On the other hand, electric pump-fed systems may actually be even more promising for the hybrid rocket systems.

Hybrid rockets have only one type of liquid propellant to feed into the combustion chamber. While this making the pressure-fed hybrid rocket systems simpler due to reduced tank volume and piping, it complicates the system design if turbopump is decided to be employed. The biggest advantage of hybrid rocket technology is the low development costs and times by being a simpler system. Turbopumps jeopardize this advantage by introducing additional complexity. All flown and tested hybrid rocket to this day uses pressure-fed systems. Nevertheless, the emerging electric pump-fed system also got hybrid rocket community's attention as well.

Casalino and Pastrone suggested the advantage of using electric pump-fed hybrid rockets by performing comparative performance tests with pressure-fed systems along with hybrid rocket motor optimization [Casalino and Pastrone, 2010]. Another system study is conducted by the author of this thesis on an upper stage hybrid rocket propulsion system by employing genetic algorithm and performance enhancements for the electric pump-fed system [Gegeoglu et al., 2018].

As will be mentioned in detail in the following section that electric pump-fed systems offer substantial advantages over conventional feed systems. Despite the fact that performance analysis is done comprehensively, it relies on the present data about the propellant pumps used in launch vehicles. For small satellite launch applications, thrust and flow rate requirements are much lower than the systems present in literature. For this reason, a pump design is proposed for a medium thrust level hybrid rocket stage and a comparative weight analysis with respect to the pressure-fed system is presented with a better accuracy. In this thesis, the author aims to strengthen the argument about relative performance advantages of electric pump-fed hybrid rockets over pressure-fed hybrid rockets through pump development processes and a comprehensive performance analysis. In the next chapter, a more detailed literature survey will be discussed for the current level of studies. In Chapters 3 and 4, pump hydraulic concepts will be introduced and a design procedure will be explained. This design procedure will be applied to the prototype design. After the preliminary design, a pump model will be created and the system-level design of the propulsion system along with the pump drive system design will be made in Chapter 5. In Chapter 6, a CFD analysis method for the pump is developed. The validation of the CFD method which was achieved by conducting tests on an industrial pump is also discussed in Chapter 5. After that, a comprehensive performance analysis will be undertaking with hybrid rocket motor and propellant feed system design. In the final chapter of this thesis, the results will be discussed and further improvements will be acknowledged.

Chapter 2

LITERATURE REVIEW

The concept of driving flight-weight pumps with electric motors is not very new. Electric motors have been employed in satellites to drive propellant pumps of on-board propulsion system. As in the case of a geostationary satellite, pumps with a very low flow rate and specific speed are driven by an electric motor for apogee propulsion [Johnsson and Bigert, 1990]. A schematic of the mentioned system is illustrated in Figure 2.1.

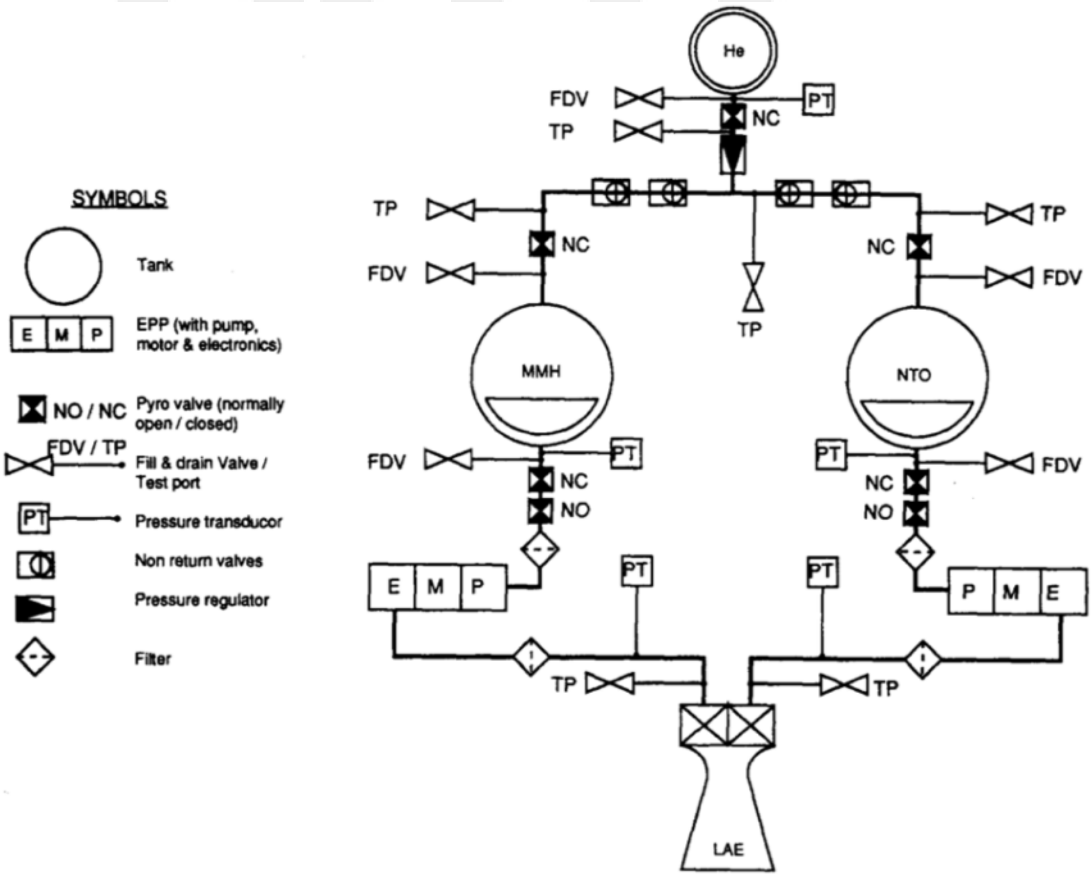

Figure 2.1: Schematic of on-board electric pump-fed liquid propulsion system [Johnsson and Bigert, 1990].

The proposed system is addressed as “Electric Propellant Pump System (EPPS)” and used MMH and NTO combination to supply propellants to the liquid rocket combustion chamber. The use of an electric pump instead of pressurizing tanks with helium caused a decrease of tank pressure from 20 bar to 5 bar and decrease in weight by 50 kg for a 2000 kg payload reportedly. Overall operational values of the pumps are presented in Table 2.1. Low power requirements due to low flow rates

Table 2.1: Design requirements of propellant pumps [Johnsson and Bigert, 1990].

	MMH	NTO
Mass Flow Rate (kg/s)	0.313	0.641
Outlet Pressure (bar)	18.70	16.90
Inlet Pressure (bar)	3.4	3.4

made electric pump-fed system viable but electrical machines still were not qualified for high power systems such as propellant pumps of a launch vehicle stage.

With the current technological advancements in electrical drive systems such as electric motors, power electronics, and batteries, high power electrical drive systems became adequately compact and light-weight to be used in space applications. Since electrically driven pump-fed systems have been introduced as an alternative propellant feed system, there has been a number of comparative studies to evaluate electric pump feed system performance over conventional feed systems.

Solda and Lentini proposed an electric pump-fed propellant feed system for a liquid rocket motor to be used for orbit insertion of a 3000 kg payload as a base case. A weight calculation of the components is done with respect to operational parameters such as combustion chamber pressure and burn time. Presented results show the advantage of the proposed approach in high combustion chambers and long burn times [Solda and Lentini, 2008]. In Figure 2.2 solid line represents the pressure-fed system while dashed lines represent electric pump-fed systems with 1000 kg, 3000 kg and 10 000 kg payloads(1000 being short-dashed line and 10 000 kg being the with the longest dash.

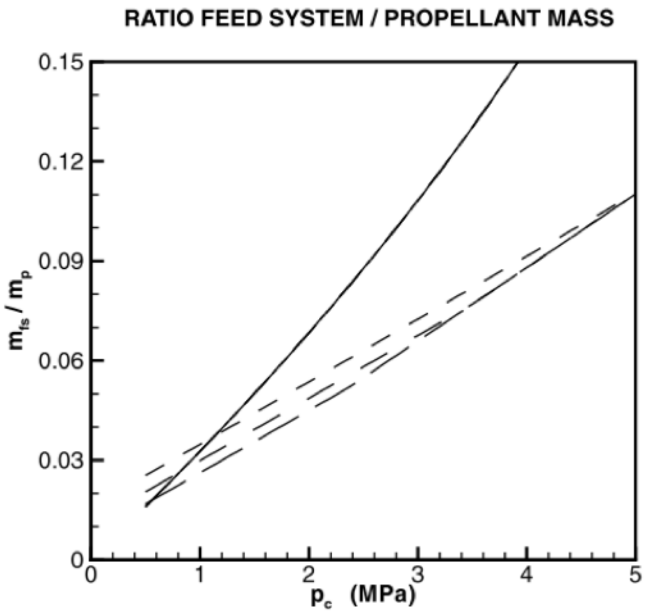

Figure 2.2: "Ratio of feed system mass over total propellant mass as a function of chamber pressure for $p_{presstank}$ =20 MPa and t_b=1000 s" [Solda and Lentini, 2008].

Parameters used to calculate electric pump system weight are assumed conservatively to avoid any biased results.

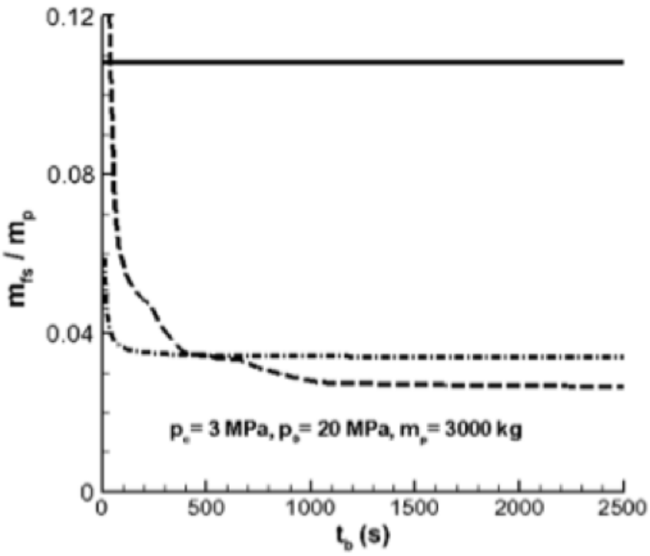

Figure 2.3: Ratio of propellant feed system mass to payload mass with respect to burn time. Solid line, pressure-fed system; dashed-dotted line, turbo pump-fed system; dashed line, electric pump-fed system [Rachov et al., 2013].

A similar study by Rachov et. al. is conducted for liquid rockets to compare electric pump system to pressure-fed and turbopump-fed systems. Components weights are calculated in a similar manner with the pump power density data "extrapolated from the Titan turbopump data" and electric motor and battery power density values taken from manufacturers. Results were parallel with previous research and a substantially reduced ratio of feed system mass to propellant mass is presented with longer burn times(See Figure 2.3) [Rachov et al., 2013].

A battery selection strategy is also given with respect to the burn time. While Li-Po batteries are suggested to be optimal in short duration and high power applications, Li-Ion a Li-S batteries that are energy-intensive presented to be more advantageous in longer burn time (See Figure 2.4.

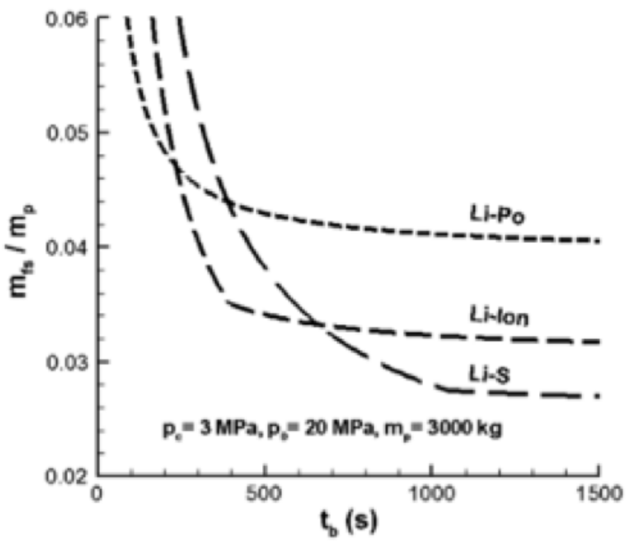

Figure 2.4: Ratio of propellant feed system mass to payload mass with respect to burn time for electric pump-fed system powered by different types of batteries [Rachov et al., 2013].

In a more detailed analysis Kwak et. al. also assessed electric pump-fed liquid rocket engines by comparing electric pump-fed system with gas generator cycle turbopump system. It has been first asserted that the operational complexity would be reduced with the electric pump-fed system since the ignition sequence is much simple in the proposed system (See Figure 2.5) [Kwak et al., 2018].

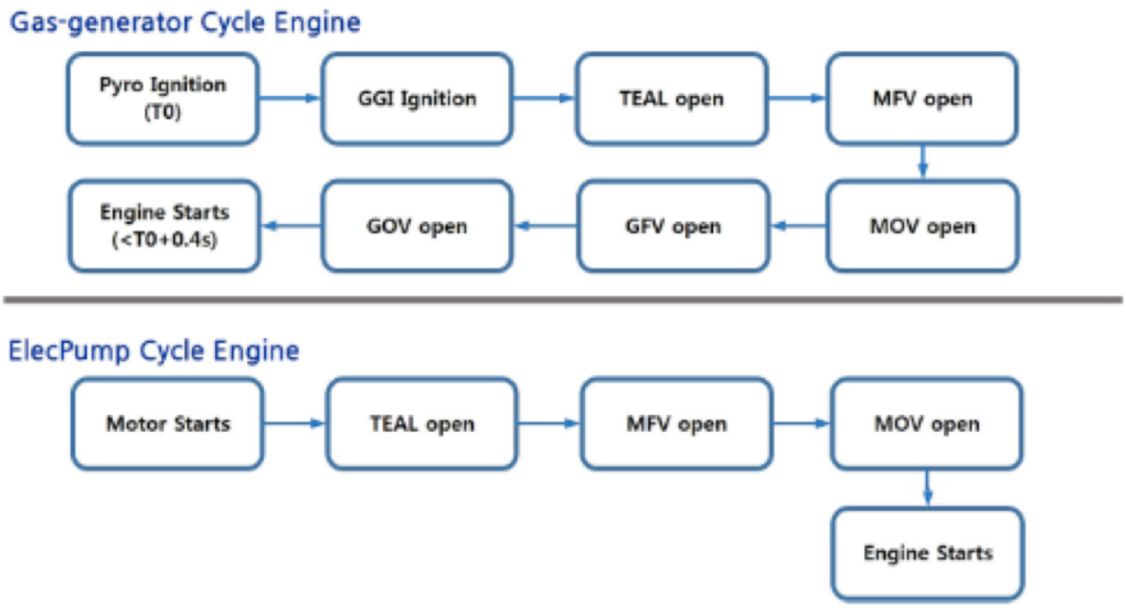

Figure 2.5: Typical ignition sequence of engines with gas generator cycle powered turbo pump and electric motor powered pump [Kwak et al., 2018].

The authors also acknowledge the power limits due to the high speeds and thermal management problems of the electric components. For the study, they assessed the systems for a low earth orbit and KLSV-II sun-synchronous orbit missions. Components' mass are obtained with the various densities obtained from the literature. As the result, a mere loss of 2-3% for payload capability is reported for LEO mission, nevertheless with increased combustion chamber pressure 3.7% payload capability increase is also found and emphasis on the simplicity of the system and reduced costs are made.

In the same year as the last paper summarized, Waxenegger-Wilfing et. al. proposed an electric pump-fed liquid rocket stage for micro-launchers for LEO and SSO applications. They have adopted a genetic algorithm (See Figure 2.6) to minimize inert mass for a given ΔV requirement. In their findings, they conclude that such a system is viable to design. Their optimization scheme resulted in low combustion chamber pressures although high chamber pressure increases the Isp. The reason of this is the increased battery and motor mass due to the high power requirements of such an option. The authors also mention the necessity of thermal management of the battery due the sensitivity of battery efficiency to environmental conditions

[Waxenegger-Wilfing et al., 2018].

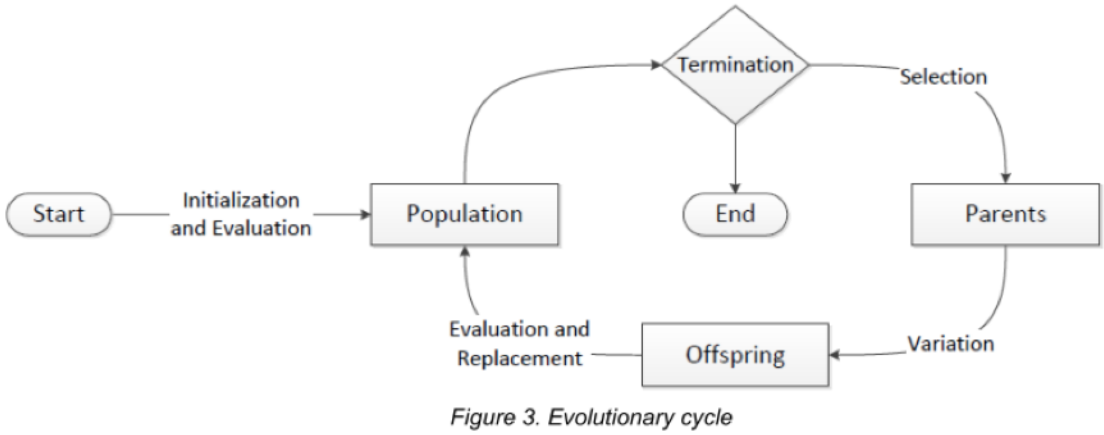

Figure 2.6: Genetic algorithm scheme implemented by Waxenegger-Wilfing et. al. [Waxenegger-Wilfing et al., 2018].

The propellant feed system is required with any given propulsion system employing liquid propellant. Most of the research about propellant feed systems are done with liquid rocket propulsion in mind due to its technological history and a wide area of application. On the other hand, hybrid rocket propulsion as an emerging technology also attracts some of the research in this subject to its field of application. As a consequence, an inevitable query for electric pump technology is investigated for hybrid rocket applications as well.

Casalino and Pastrone considered the proposed system to be employed on PE / H_2O_2 third stage hybrid rocket motor with multi-port grain geometry. A "nested direct/indirect optimization procedure" is carried out for motor and trajectory optimization and the required feed system weight is calculated parametrically. 6 combinations of optimized system are considered with port configuration of 6 and 8 port and with blow-down, pressure-fed and electric pump-fed propellant feed system options. In the reported data, the electric pump-fed system's payload mass resulted in a higher value compared to the other feed system in both port configurations. The electric pump-fed configuration also exhibited higher Isp and lower thrust value, which implies the system is optimized with a longer burn time [Casalino and Pastrone, 2010].

Casalino et. al. continued the research presented above and presented another optimization procedure employing particle swarm optimization technique. Electric pump-fed system with electric motor and pump properties of current technology and with anticipated enhanced values are assessed by two separate versions and they are compared with the pressure-fed system. Results showed about %12 percent payload increase for the 2000 kg payload class [Casalino et al., 2019].

In previous research of the author of this thesis, an extensive system study is undertaken on Paraffin/LOX upper stage hybrid rocket with pressure fed and electric pump-fed propellant feed systems and a genetic algorithm is used to find the optimal points of both systems restricted with 100 kg of payload and 1 MNs of total impulse [Gegeoglu et al., 2018].

In the research, an internal ballistic model is created for hybrid rocket combustion with paraffin/LOX propellant combination and the feed system weight model is setup. Optimizing parameters are chosen to be combustion chamber pressure, average O/F ratio, burn time and pressurization tank initial pressure. Each parameter value is converted into binary format then these numbers are concatenated to form a genome of the candidate combination. Then the population is initialized with a random selection of parameters with their performance data chosen as the ΔV capability. The population is evolved by randomly pairing candidate systems and eliminating the worse performing system from the population. After the elimination phase, remaining genomes are paired again to reproduce offspring by randomly selecting parent gene blocks to form a new combination. The algorithm works very much like the evolutionary mechanism. This procedure is applied for pressure-fed and electric pump-fed systems in separate populations. After 30 generations, histograms of each gene distribution in the population for both systems are presented [Gegeoglu et al., 2018].

Results showed that the electric pump-fed system is optimized for longer burn times than pressure fed systems. And at optimum combination, the electric pump-fed system exhibited %6.6 more ΔV capability than the pressure fed system [Gegeoglu et al., 2018].

As a follow-up study for the research mentioned, a more detailed analysis is undertaken to partly eliminate the ambiguity in assessing pump mass in [Gegeoglu et al., 2019]. In previous analysis of all authors asserting the advantage of electric pumps on rockets, pump mass was calculated from an average power density, that is the hydraulic power capability per unit mass, collected from rocket turbo-pump manufacturer data-sheets. This approach is believed to be inadequate since pump weight does not increase linearly by the hydraulic power and scaling effects are hard to predict. Extrapolating the data of large pumps used on heavy launch vehicles to small to medium scale pumps introduces a bias towards higher pump power density. For this reason, a study for electric pump design tailored for a hybrid rocket upper stage application similar to what is mentioned in [Gegeoglu et al., 2018] is pursued.

A pump design for 5.8 kg/s of LOX flow rate with 40 bar of differential head is done. Impeller and volute designs are made according to the existing design guidelines for centrifugal pump design. A speed limit for the electric motors readily available off-the-shelf is taken as a constraint. Due to the very low specific speeds obtained from off-the-shelf electric motor speeds and low flow rates, as a design strategy, a high head double-stage and a low head single-stage pump designs are pursued. Impeller and volute calculations are done only for a single-stage option and a geometry is created. After this, a CFD analysis is made for the pump and results are presented. A suitable casing is also modeled in CAD environment (See Figure 2.7) to determine the approximate pump mass [Gegeoglu et al., 2019].

Figure 2.7: CAD model of the pump [Gegeoglu et al., 2019].

It's been stated that the previous power density assumptions used were indeed overstated for a small pump. With the corrected mass data for pump and more recent data for electric motor and batteries, a propellant feed system weight analysis is made for a pressure-fed, partially pressure-fed with single-stage pump and a sole double-stage pump system. Results clearly show not only the advantage of employing electric-pump in feed system for the selected propulsion system but also the marginal benefit of using electric-pumps by the evidence of weight advantage in a partially pressure-fed single-stage pump [Gegeoglu et al., 2019].

This thesis is to bolster the fidelity of the findings of previous research and to provide a design procedure for developing an electric pump.

Chapter 3

PUMP HYDRAULICS

Centrifugal pumps convert mechanical energy to hydraulic energy by adding enthalpy to the fluid that goes through the impeller. The amount of head that impeller is putting onto the working fluid is found by applying the conservation of angular momentum in a one-dimensional approach. In the one-dimensional approach, fluid is considered to pass stations that are numbered from the inlet of the pump to the outlet of the pump.

When studying the flow through impellers, a graphical representation of velocity vectors is often used. These representations are called velocity triangles and they consist of absolute flow velocity c, blade tangential velocity u and relative velocity of flow with respect to the blade w. An example of such representation is given in Figure 3.1.

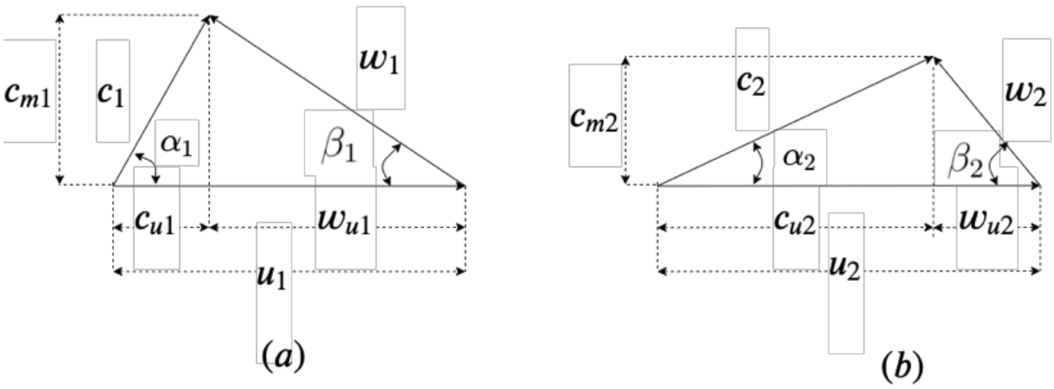

Figure 3.1: a) Inlet velocity triangle, b) Outlet velocity triangle[Stepanoff, 1957].

3.1 Definition of parameters and dimensionless coefficients

Pumps are hydraulically complex machines. It is difficult to compare different models having different working fluid, 3-dimensional flow characteristics and geometry. Because of that, some performance and identifying dimensionless parameters have been introduced to classify different types of pumps and their capabilities.

3.1.1 Head

Head is defined as the measure of the height of the fluid column where hydrostatic pressure at the bottom of the column matches the fluid pressure.

$$H = \frac{P}{\rho g_0} \tag{3.1}$$

The head is called static or total head when static or total pressure is represented respectively. This definition helps to compare pumps working with different density fluids since a pump's head capability is almost the same (despite some minor differences due to disparate viscosities) with a certain geometry, speed, and flow rate.

3.1.2 NPSH

NPSH (Net Positive Suction Head) is the head value corresponding to the pressure difference between the total pressure and saturation pressure of the fluid.

$$NPSH = \frac{p_{tot} - p_v}{\rho g} \tag{3.2}$$

Pumps move fluid from the reservoir to the pump inlet by a pressure difference. This is caused by lowered static pressure at the impeller of inducer inlet due to high relative velocities. NPSH is directly linked to the suction capability of the pump since if pressures lower than saturation pressure of fluid are present on the blades, cavitation occurs and that can cause a decrease in performance and increase in radial loads and vibration.

There are different NPSH definitions with different subscripts according to their proper usage. NPSH_A means available NPSH that is the NPSH calculated with fluid's current total pressure. NPSH_R value is the required NPSH that is the least amount of NPSH that is allowed by the designer. This value is often set to different cavitation conditions at the blade leading edge denoted by subscripts i or x. NPSH_i is related to reservoir pressure where cavitation incidence occurs at the blade inlet. NPSH_x is the NPSH value where the pump head is reduced by x% compared to non-cavitating conditions. Usual NPSH_x value used in practice is NPSH_3 and NPSH_A value is set to this value.

3.1.3 Specific speed

As explained in chapter 3.4 in the referenced textbook, “Turbulent flows in complex geometries cannot be described accurately by simple analytical means. In practice, such flows are treated with similarity characteristics (“model laws”) and dimensionless coefficients by means of which test results can be generalized and applied for prediction purposes in new applications” [Gülich, 2010]. For this purpose, a parameter called specific speed is defined by using operational parameters of the pump consisting head, rotational speed, and volumetric flow rate.

Statistical correlations between specific speed and the behavior of pumps have been found by empirical results in a few standards throughout history. There are 3 main definitions of specific speed that are used to correlate and predict the performance of the pump. In imperial units, specific speed is defined as

$$N_s = \frac{N\sqrt{Q}}{H^{3/4}} \tag{3.3}$$

Where N is the rotational speed in rev/min (rpm), Q is the volumetric flowrate in gpm and H is the differential head in feet.

In SI units there are 2 widely used definitions with a slight difference in formulations. The first and more commonly used one follows as

$$n_q = \frac{N\sqrt{Q}}{H^{3/4}} \tag{3.4}$$

Where N is in rpm, Q is in m^3/s and H in m. The latter one is defined as

$$n_s = \frac{\omega\sqrt{Q}}{H^{3/4}} \tag{3.5}$$

Where ω is the angular velocity in rad/s, Q is in m^3/s and H is in m while g_0 is the gravitational acceleration. Pumps in different sizes with the same specific speed have similar geometries and flow fields which makes it easy to scale operational parameters.

3.1.4 The Suction Specific Speed

The suction specific speed is defined to compare suction capabilities of pumps that are not geometrically similar and is formulated as

$$N_{ss} = \frac{N\sqrt{Q}}{NPSH^{3/4}} \tag{3.6}$$

This parameter is defined at the best efficiency point and for the shockless entry conditions where the volumetric flow rate results in zero flow incidence at the blade inlet. NPSH value is usually taken as $NPSH_3$ conventionally.

3.1.5 Head and flow coefficients

When performance data of the pump is illustrated graphically, it is often useful to non-dimensionalize the variables H and Q. This gives the designer the advantage of comparing different pumps with different sizes and speeds or withholding propriety data when presenting the performance data.

Head coefficient is the non-dimensional head parameter with respect to circumferential speed at the impeller outlet and it follows as

$$\Psi = \frac{gH}{u_2^2/2} \tag{3.7}$$

Flow coefficient, on the other hand, is used to non-dimensionalize the flow rate with respect to tip speed at the LE and TE of the blades. Flow coefficients are defined at the inlet and outlet of the blades with respective meridional velocities and tip speeds. Since meridional velocity is directly related to Q, it is appropriate for interpreting flow coefficients as the volumetric flow rate. Inlet and outlet flow coefficients are defined in equations 3.8 and 3.9.

$$\phi_1 = \frac{c_{1m}}{u_1} \tag{3.8}$$

$$\phi_2 = \frac{c_{2m}}{u_2} \tag{3.9}$$

3.1.6 Cavitation coefficients

When there is a need to develop a similarity law regarding the cavitation performance of geometrically similar pumps, a cavitation coefficient must be established. This coefficient is defined as

$$\sigma_x = \frac{NPSH_x}{u_1^2/2g} \tag{3.10}$$

and this coefficient links different impellers with similar geometry but different speeds and dimensions to make scaling laws for inlet design convenient for the designer [Gülich, 2010].

3.2 Theoretical Head

The conservation of angular momentum is established on the mass flowing through the impeller. Change in the momentum of fluid is equated to the sum of all torques acting on the fluid.

$$T = \frac{dm}{dt}(r_2 c_2^{'} cos\alpha_2 - r_1 c_1^{'} cos\alpha_1) \tag{3.11}$$

By substituting mass flow rate and multiplying both sides with angular velocity the equations yields as,

$$T\omega = \frac{Q\rho}{g}\omega(r_2 c_2^{'} cos\alpha_2 - r_1 c_1^{'} cos\alpha_1) \tag{3.12}$$

Where $T\omega$ is the power that is applied to the fluid by the impeller. This power term is ideally used to increase the pressure of the fluid without any loss and that head rise due to this exchange is called as ideal head or input head. And noting that $\omega r = u$ and $c\ cos\alpha = c_u$

$$Q\rho H = \frac{Q\rho}{g}\ (u_2 c_{u2}^{'} - u_1 c_{u1}^{'}) \tag{3.13}$$

If the inlet flow is axial, ($c_{u1} = 0$), ideal head in 3.13 is maximized.

$$H_i = \frac{u_2 c_{u2}^{'}}{g} \tag{3.14}$$

3.3 Euler's Head

When velocity triangles are drawn in a way that the flow angles correspond to the actual blade angles (meaning there is no slip in either edge), the ideal head calculation yields a greater head than input head. But in practice, actual absolute flow angles are not the same with the blade angles. To avoid confusion, the head calculated from the velocities based on actual blade angles is referred to as Euler's Head. The difference between the actual velocity triangle and Euler's velocity triangle is shown in Figure 3.2.

$$H_e = \frac{u_2 c_{u2}}{g} \tag{3.15}$$

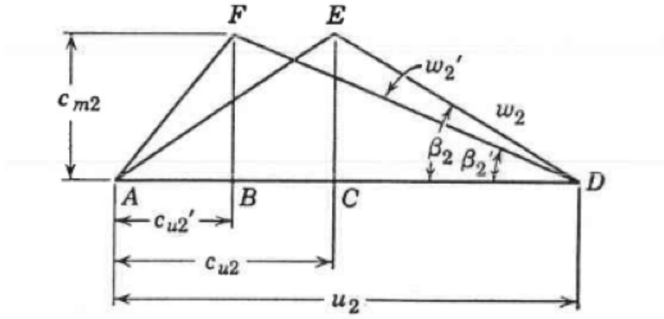

Figure 3.2: Euler's velocity triangle[Stepanoff, 1957].

3.4 Slip Factor

The difference between the input head and Euler's head comes from a phenomenon occurs in the passage between impeller blades. This phenomenon is called "slip" and explained in chapter 3.3 of [Gülich, 2010]. Blades exert force on the fluid by imposing disparate flow field at the front and back faces of the blades. These faces are called pressure side and suction side of the blade and because of the different flow fields occur on these faces, flow cannot exactly follow the blade. When the flow is leaving the blade, the absolute flow angle is smaller than the blade exit angle. An illustration of the case is shown in Figure 3.3.

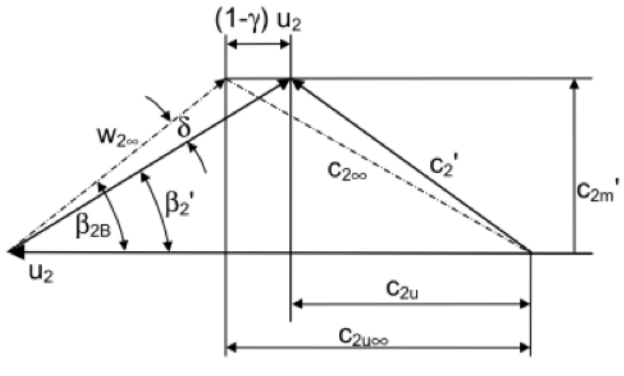

Figure 3.3: Slip velocity representation on velocity triangle triangle, extracted from [Gülich, 2010].

The circumferential velocity difference between the actual flow and the "blade-congruent" flow is called the slip velocity. To find this velocity, an equation containing a "slip factor" is established [Gülich, 2010].

$$c_{2u} - c'_{2u} = (1-\gamma)u_2 \tag{3.16}$$

From 3.16 slip factor is obtained by using the relation $tan\beta_{2B} = c'_{2m}/(u_2 - c_{2u})$

$$\gamma = 1 - \frac{c_{2u} - c'_{2u}}{u_2} = \frac{c'_{2u}}{u_2} + \frac{c'_{2m}}{u_2 tan\beta_{2B}} \tag{3.17}$$

Superscript ' denotes a velocity value incorporating blade blockage due to finite thickness of blades and a blade blockage factor is introduced.

$$\tau_i = \left(1 - \frac{e_i Z_i}{\pi D_i sin\beta_{iB} sin\lambda_i}\right)^{-1} \tag{3.18}$$

where $i = 1$ for impeller inlet and $i = 2$ for impeller outlet calculations.

There has been a number of studies to investigate and analytically determine slip in impellers. Wiesner gave a review of past studies and recommended Busemann's model for slip factor as a more general relation for this phenomenon [Wiesner, 1967].

$$\gamma = \mathrm{f}_1 \left(1 - \frac{\sqrt{sin\beta_{2B}}}{Z_2^{0.7}}\right) k_w \tag{3.19}$$

where f_1 is 0.98 for radial impellers and k_w is the influence of inlet diamater on slip.

$$k_w = 1 - \left(\frac{D_1/D_2 - \epsilon_{lim}}{1 - \epsilon_{lim}}\right)^3 \tag{3.20}$$

And k_w is 1 for $D_1/D_2 < \epsilon_{lim}$ and ϵ_{lim} is the solidity limit defined as

$$\epsilon_{lim} = e^{-\frac{8.16 sin\beta_{2B}}{Z_2}} \tag{3.21}$$

Chapter 4

METHODOLOGY

4.1 Pump Design

In this thesis, a design of a hydraulic pump is conducted with two different approaches. One is a design procedure of Gulich [Gülich, 2010] using cascade and channel flow models together with empirical correlations to create a robust analytical method. The other design procedure suggested by Stepanoff [Stepanoff, 1957], is a more empirical guideline with design coefficients found over a vast number of tests. This empirically-based design method explained in [Stepanoff, 1957] and the analytic approach of Gulich are both employed in designing the pump and their methodology is explained in the next subsection.

For a structured design procedure, the main dimensions should be obtained before going into the detailed design of flow channel and blade geometry. Nevertheless, before any of these steps, target specifications regarding the head, flow rate and speed must be chosen.

4.1.1 Target Quantities

Before starting to design process, operational requirements must be established. A volumetric flow rate and the differential head are chosen for the pump and this pair is set as the design point. Since these values are to be employed for most of the operation time of the turbomachine, the point described by these values should be the best efficiency point of the machine. Therefore H and Q values become optimum values and referred to as H_{opt} and Q_{opt}.

The speed of the impeller is usually determined by the pump drive capabilities and suction performance.

After determining these 3 parameters, specific speed is calculated to specify the type of the impeller and the pump. Varying impeller types such as axial, radial and mixed flow are classified from statistical data by specific speeds as illustrated in Figure 4.1.

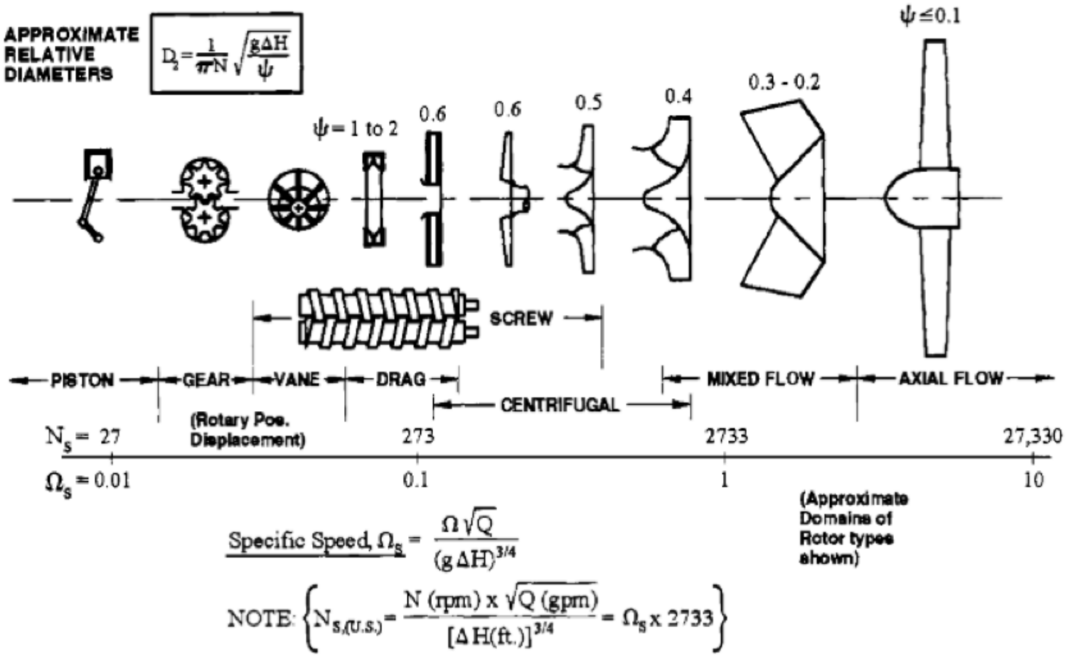

Figure 4.1: Different pump types by different specific speeds [Karassik, 1976].

4.1.2 Efficiencies

Efficiencies are assumed from statistical data where efficiency can be estimated with the design requirements according to [Gülich, 2010]. Best fit correlations resulted in different formulations for pumps with different types and with a different number of stages. Therefore only the correlations for radial single-stage pumps are provided below as the intended pump will be a single-stage radial type.

Optimal overall efficiency is estimated from Eq. 4.1.

$$\eta_{opt} = 1 - 0.0095 \left(\frac{Q_{ref}}{Q}\right)^m - 0.3 \left(0.35 - \log\frac{n_q}{23}\right)^2 \left(\frac{Q_{ref}}{Q}\right)^{0.05} \tag{4.1}$$

where,

$$m = 0.1a \left(\frac{Q_{ref}}{Q}\right)^{0.15} \left(\frac{45}{n_q}\right)^{0.06} \tag{4.2}$$

And optimal hydraulic efficiency is estimated from Eq. 4.3.

$$\eta_{h,opt} = 1 - 0.055 \left(\frac{Q_{ref}}{Q}\right)^m - 0.2 \left(0.26 - \log\frac{n_q}{25}\right)^2 \left(\frac{Q_{ref}}{Q}\right)^{0.1} \tag{4.3}$$

where,

$$m = 0.08a \left(\frac{Q_{ref}}{Q}\right)^{0.15} \left(\frac{45}{n_q}\right)^{0.06} \tag{4.4}$$

with $a = 1$ for $Q \leq 1$ m^3/s, $a = 0.5$ for $Q > 1$ m^3/s and $Q_{ref} = 1$ m^3/s.

4.1.3 Impeller Main Dimensions

In this section, determination process of impeller main dimensions is explained. Parameters calculated are illustrated on a representative sketch in Figure

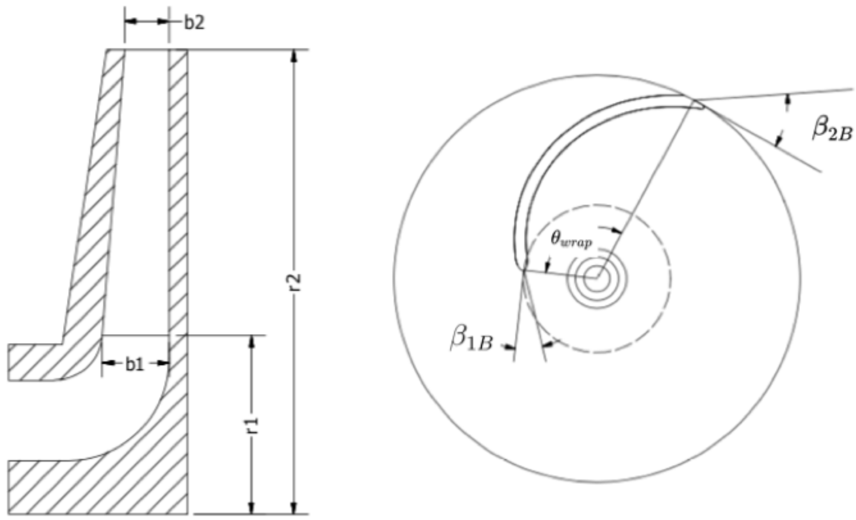

Figure 4.2: Illustration of dimensional parameters of the impeller.

Impeller Diameter

The impeller diameter is directly related to the head capability of the pump and has been correlated by statistical studies done on a large number of pumps in the industry.

One method for determining impeller diameter is given by Stepanoff with empirical design constants. For meridional speed at the exit of the impeller is defined by Equation 4.5 [Stepanoff, 1957].

$$u_2 = K_u \sqrt{2gH} \tag{4.5}$$

The coefficient K_u is read from the Figure 4.3 with the calculated specific speed. Once the circumferential velocity at the outlet of the impeller is known, the outlet

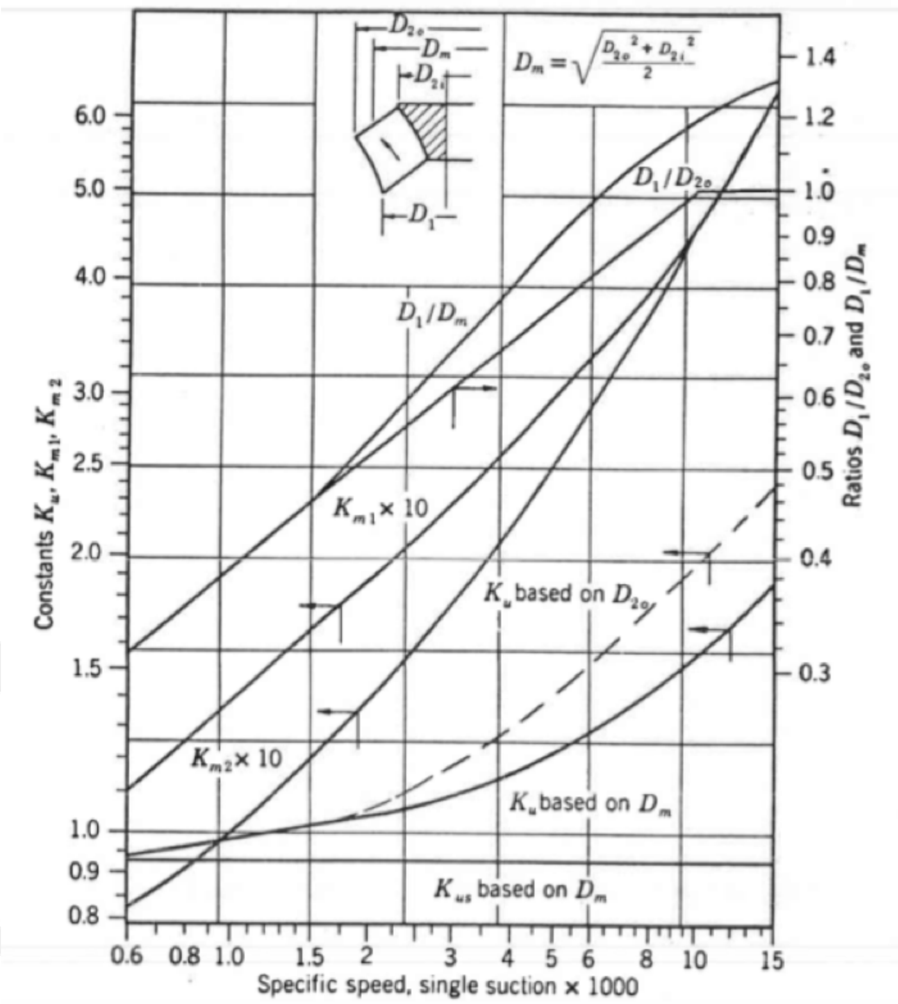

Figure 4.3: Empirical impeller constants w.r.t specific speed of the pump[Stepanoff, 1957]

diameter can easily be estimated with Equation 4.6.

$$D_2 = \frac{2\ u_2}{\omega} \tag{4.6}$$

One other procedure for selecting the impeller diameter is explained in [Gülich, 2010] uses the head coefficient at the best efficiency point (denoted by subscript *opt*) that is statistically determined with following relation.

$$\Psi_{opt} = 1.21 e^{-0.77 n_q / n_{q,ref}}, n_{q,ref} = 100 \tag{4.7}$$

Once the optimum head coefficient is found, impeller diameter is found by the equation below.

$$D_2 = \frac{60}{\pi n} \sqrt{\frac{2 g H_{opt}}{\Psi_{opt}}} \tag{4.8}$$

Inlet Diameter

Inlet diameter of the impeller is referred to as the diameter at the blade inlet tip. This dimension is found by Stepanoff with the same procedure by reading the diameter ratio D_1/D_2 from 4.3. Gulich proposed alternative methods to determine the inlet diameter of the impeller. Among those, one method is thought to be more convenient, less uncertain and more coherent to the method used to determine impeller diameter D_2. Other methods require determining multiple coefficients that are widely scattered and not very robust with low specific speed. Therefore the following correlation with the estimated optimal head coefficient is used.

$$\frac{D_1}{D_2} = f_{d1}\sqrt{\left(\frac{D_n}{D_2}\right)^2 1.48x\Psi_{opt}\frac{n_q^{1.33}}{(\eta_{\mathrm{v}}\delta_{\mathrm{r}})^{0.67}}} \tag{4.9}$$

where,

$$\delta_{\mathrm{r}} = 1 - \frac{c_{1m}}{u_1 \mathrm{tan}\alpha_1} \tag{4.10}$$

and f_{d1} is between 1.15 and 1.05 decreasing from $n_q = 15$ to 40.

Outlet Blade Width

Outlet blade width can be found indirectly by estimating outlet meridional velocity c_{2m} with empirical design constant K_{m2} in 4.3.

$$c_{2m} = K_{m2}\sqrt{(2gH)} \tag{4.11}$$

Latter procedure follows the conservation of mass rule.

$$Q = c_{2m} * A_2 \tag{4.12}$$

where A_2 is the area fluids flow through at the outlet of impeller. It should be noted that blade thickness at the outlet causes an area reduction for the flow. The expression for outlet area is written as the following.

$$A_2 = \pi b_2 D_2 - \frac{Z_2 e_2}{sin\beta_2 sin\lambda_2} \tag{4.13}$$

Where Z_2 is the number of blades at the outlet of the impeller (Specified with subscript 2 in case of a design with splitter blades), b_2 is the outlet blade angle and λ_2 is the twist angle at the outlet. λ_2 is 90° when blades are cylindrical (extruded parallel to the rotation axis). Outlet blade width b_2 can be found from the corresponding flow area to satisfy the meridional velocity.

Gulich similarly proposes a more straight forward correlation devised from specific speed [Gülich, 2010].

$$\frac{b_2}{D_2} = 0.017+0.262\frac{n_q}{n_{q,ref}} - 0.08\left(\frac{n_q}{n_{q,ref}}\right)^2 + 0.0093\left(\frac{n_q}{n_{q,ref}}\right)^3, n_{q,ref} = 100 \quad (4.14)$$

Blade Inlet Width

Blade inlet width is found with the similar procedure explained in the previous section.

$$c_{1m} = K_{m1}\sqrt{2gH} \quad (4.15)$$

Next, the corresponding area is found by the mass conservation principle.

$$A_1 = \frac{Q}{c_{1m}} \quad (4.16)$$

At this point, one further assumption has to be made to find the blade inlet diameter. If the blade tip is perpendicular to the rotation axis, the blade inlet diameter also equals to the eye diameter. In this case blade tip on the outer streamline is on the eye wall of the impeller and the blade tip at the inner streamline is on a point close to the shaft. If blade tip is perpendicular to the rotation axis, blade inlet diameter is usually different, and greater than impeller eye diameter, and radii at the inner and outer streamline are the same or very close to each other. In low specific speed pumps, the latter case is usually present and the procedure for this case is followed since the design specific speed is low as it is explained in the following sections.

Blade inlet width is consequently calculated with blade blockage.

$$A_1 = \pi b_1 D_2 - \frac{Ze_1}{sin\beta_1 sin\lambda_1} \quad (4.17)$$

Outlet Blade Angle

Although there is no analytical rule or optimal value for the blade angle at the outlet, experiments and statistical data about the impeller in the literature suggests value between 15° to 45°.

Outlet blade angle decision should be made with great care in order to achieve the desired head coefficient and performance. Even though estimations are used in the initial design phase of the impeller, this angle (along with the inlet angle) is varied iteratively on CFD studies to determine an optimum point. Nevertheless, this angle is chosen between 20° to 25° in high head coefficient pumps.

Flow deflection is anticipated according to slip factor estimation. In order to prevent turbulent flow losses from non-uniform velocity profile at the outlet, this deflection angle should be as low as possible without compromising the head coefficient. In [Gülich, 2010], deflection angle is recommended to be kept below 14°. To check for the deviation angle, a slip factor is calculated from 3.19 and flow velocity c_{2u} is estimated.

$$c_{2u}^{'} = u_2 \left(\gamma - \frac{c_{2m}^{'}}{u_2 tan \beta_{2B}} \right) \tag{4.18}$$

Then, actual flow angle $\beta_2^{'}$ is found by

$$\beta_{2B} \theta_{wrap} = arctan \frac{c_{2m}^{'}}{u_2 - c_{2u}^{'}} \tag{4.19}$$

Leading to an approximate deviation angle $\delta = \beta_{2B} - \beta_2^{'}$

Inlet Blade Angle

Blade angles are found from the inlet velocity triangle while taking the blade blockage into account.

$$\beta_{1B} = arctan \frac{c_{1m}^{'}}{u_1 - c_{1u}^{'}} \tag{4.20}$$

Blade Thickness

Blade thickness is mostly constrained by mechanical strength and manufacturing methods. The ratio e/D_2 is suggested between 0.016 to 0.022 from experience [Gülich, 2010].

Blade thickness can also vary from leading edge to trailing edge. However, this strategy is left to the computational modeling phase.

Blade Leading Edge Profile

Blade leading edge is important in the way that it determines the flow separation zones and cavitation regions. As stated in [Gülich, 2010], 2:1 elliptical profiles lead to favorable pressure gradients, especially when extended only over a short distance.

Blade Trailing Edge Profile

There two strategies to define a blade trailing edge thickness. The first one is tapering the exit thickness to half of the blade thickness to reduce wake width and pressure pulsations. The other is to preserve the thickness in case of a head deficit [Gülich, 2010].

Blade Wrap Angle

Blade wrap angle θ_{wrap} determines the blade shape along with inlet and outlet diameter. This value is either is set to a value so blade angle distribution from inlet to outlet is subject to variation, or a blade angle distribution is selected so wrap angle is elf determined. This determination process is used in impeller optimization which is not in the scope of this thesis. Therefore a widely used value of 120 degrees is used for the design.

4.1.4 Volute Main Dimensions

The volute of the pump collects the flow with high circumferential velocities and directs it to the discharge pipe while decelerating it and recovering as much dynamic pressure it can to static pressure which is required for the system.

For the shape of volute cross-sections, ease and convenience in design and manufacturing should also be considered. Rectangular cross-sections offer the advantage of such conveniences, therefore this type of cross-sections are chosen for design [Gülich, 2010]. An illustration for the definition of parameters calculated in this subsection is presented in Figure 4.4.

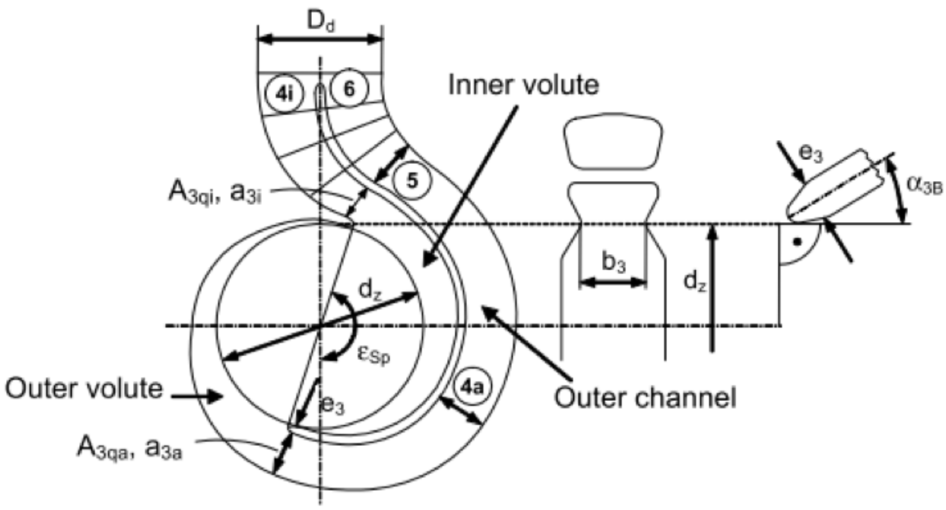

Figure 4.4: A cross section of a double volute. Base circle diameter D_3 is shown as dz in the figure [Gülich, 2010].

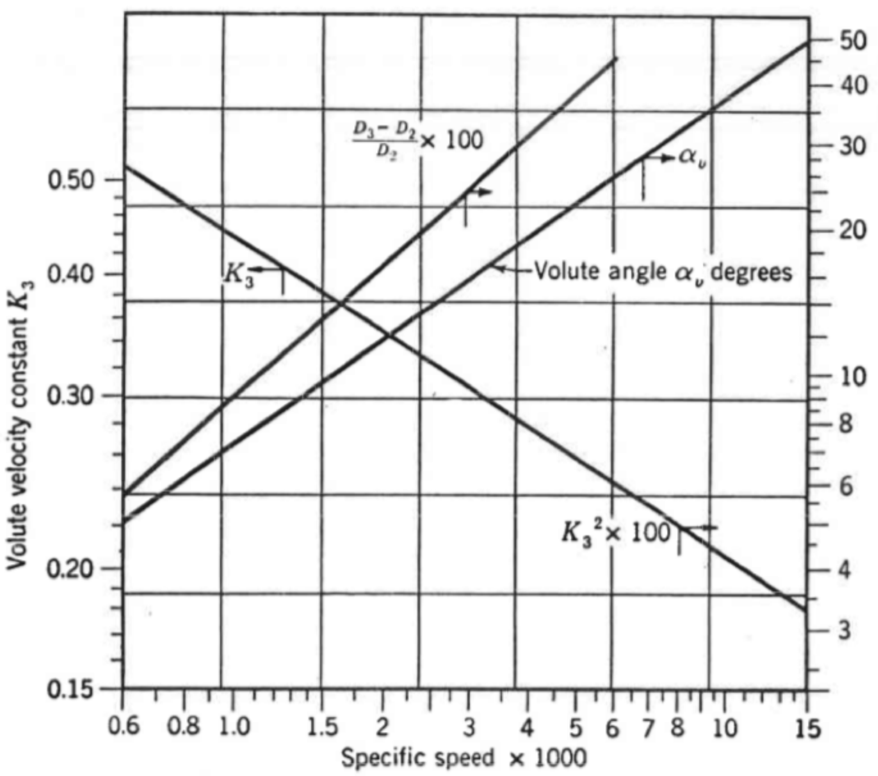

Figure 4.5: Empirical volute constants w.r.t specific speed of the pump [Gülich, 2010].

Volute Base Circle Diameter

For main dimension calculations of the volute, Stepanoff introduced empirical coefficients to apply in the preliminary design phase of the pump (See Figure 4.5) [Stepanoff, 1957].

Volute base circle diameter can be found by reading value for the volute base percentage $\frac{D_3-D_2}{D_2}$x100 .

Gulich similarly introduces a guideline for volute calculations from empirical correlations. For reduced pressure pulsations, a permissible distance between the impeller and volute cutwater has to be present [Gülich, 2010].

$$\frac{D_3}{D_2} \geq 1.03 + 0.1\frac{n_q}{n_{q,ref}} + 0.07\frac{\rho H_{st}}{\rho_{ref} H_{ref}} \tag{4.21}$$

where $n_{q,ref} = 40$, H_{ref} =1000 m and $\rho_{ref} = 1000$ kg/m^3.

Volute Channel Width

Volute channel width is adjusted for a smooth transition from volute throat to diffuser section that requires volute throat crossection to be close to a square. Therefore large b_3 values are required. Gulich there suggests 2.0 to 4.0 for b_3/b_2 ratios in low specific pumps [Gülich, 2010]. Stepanoff suggest b_3/b_2 ratio around 2.

Volute Cutwater Profile

Volute cutwater according to [Gülich, 2010] must be profiled elliptically to establish low sensitivity to the flow incidence. The tip of the cutwater is advised to be a circle with a diameter of $0.02D_2$.

Volute Cutwater Angle

The cutwater section of the volute usually has a small angle towards the impeller to collect to flow effectively. This angle α_3 is also read from the Figure 4.5 referred as α_v.

In [Gülich, 2010], this angle is calculated from the velocities with a limited incidence angle.

$$\alpha_3 = arctan\frac{c_{3m}}{c_{3u}} \tag{4.22}$$

where,

$$c_{3m} = \frac{Q}{\pi d_3 b_3} \tag{4.23}$$

and from the conservation of angular momentum,

$$c_{3u} = \frac{c_{2u} D_2}{D_3} \tag{4.24}$$

Volute cutwater angle α_{3B} is then established by taking some incidence into account by,

$$\alpha_{3B} = \alpha_3 + i \tag{4.25}$$

where $i = \pm 3°$.

Volute Throat Section

Volute throat section for rectangular shaped volutes consists of a rectangle with a width of b_3 and a height of a_3. After determining b_3, a_3 determined as the pitch of the spiral starting from the base circle and ending at the cutwater with the following equations according to [Gülich, 2010].

$$r_a = r_z^{'} X_{\mathrm{v}} \tag{4.26}$$

where $r_z^{'}$ is the radius of outer point of the cutwater ($r_z^{'} = r_z + e_3/2$) and X_{v} is the factor defined as

$$X_{\mathrm{v}} = e^{\frac{Q}{b_3 c_{2u} r_2}} \tag{4.27}$$

a_3 is then found by

$$a_3 = r_a - r_z^{'} \tag{4.28}$$

An alternative approach from [Stepanoff, 1957] suggests a velocity calculation at the volute throat followed by an area calculation by using the conservation of mass principle. Volute velocity in the cutwater region c_3 can be found by

$$c_3 = K_3\sqrt{2gH} \tag{4.29}$$

$$A_{3q} = \frac{Q}{\rho c_3} \tag{4.30}$$

Therefore with the selected b_3 value, $a_3 = A_{3q}/b_3$ can be found for a rectangular volute.

4.2 Hybrid Rocket Motor Design

To establish a firm ground for the advantage of the proposed electric pump-fed feed system over the conventional pressure-fed system, a hybrid rocket propulsion system is needed to be designed in order to be able to quantify the relative advantages of the electric pump system. In this regard, the procedure along with the fundamental aspects of rocket propulsion, especially for hybrid rockets, is outlined in this section.

4.2.1 Hybrid Rocket Propulsion Fundamentals

For a rocket to achieve its target thrust, it should expel the mass with an equal momentum as established by equation 1.1. In the mentioned equation, V_e term is the exit velocity of the mass exiting from the nozzle and it has two contrıbtıon factors. One of them is related to combustion characteristics and called characteristic velocity (c^*). The other comes from the isentropic compressible flow in the nozzle and denoted by thrust coefficient(C_F)

$$V_e = c^*\ C_F \tag{4.31}$$

$$c^* = \sqrt{\frac{R\ T_{ch}}{\gamma[2/(\gamma+1)]^{(\gamma+1)/(\gamma-1)}}} \tag{4.32}$$

Characteristic velocity can also be found by using the choked flow condition at the ideal nozzle throat with the following expression.

$$c^* = \frac{p_{ch} A^*}{\dot{m}} \tag{4.33}$$

$$C_F = \sqrt{\frac{2\,\gamma^2}{\gamma-1}\left(\frac{2}{\gamma+1}\right)^{(\gamma+1)/(\gamma-1)}\left[1-\left(\frac{p_e}{p_{ch}}\right)^{(\gamma-1)/\gamma}\right]} + \frac{p_e - p_a}{p_{ch}}\frac{A_e}{A^*} \tag{4.34}$$

The parameters c^* and C_F are dependent on the ratio of specific heats and molecular weight of the product species. Therefore these parameters are calculated with the help of NASA CEA(Chemical Equilibrium Application), a thermochemical calculator that solves the chemical equilibrium inside an ideal combustion chamber and ideal nozzle.

Regression Rate

In hybrid rockets, oxidizer flows through a port in the solid fuel grain and forms a boundary layer combustion near the port walls.

Oxidizer molecules in the core of the stream and vaporized fuel molecules near port walls get transported to the combustion layer to feed the combustion process. A part of the heat generated by this exothermic reaction vaporizes fuel and this process results in a regression of the port wall due to mass loss from the surface. This phenomenon largely determines the internal ballistic characteristics of the motor.

Karabeyoglu et. al. investigated this regression behavior and presented a relation between the oxidizer mass flux and the regression rate for the selected propellant combination. The regression rate is described by the equation [Karabeyoglu et al., 2007].

$$\frac{dr}{dt} = aG_{ox}^n \tag{4.35}$$

where G_{ox}^n is the oxidizer mass flux described by equation 4.36, and the parameters a and n are propellant combination specific coefficients.

$$G_{ox} = \frac{\dot{m}_{ox}}{A_p} \tag{4.36}$$

In [Karabeyoglu et al., 2002], Karabeyoglu et. al. introduced "liquefying fuels" and liquid "droplet entrainment" phenomena to overcome the drawback of low regression rate behavior of solid fuels for high-performance applications. In another research Karabeyoglu et. al. conducted research on regression rate of paraffin wax and suggested $a_n = 0.488$ and $n = 0.62$ [Karabeyoglu et al., 2004].

4.2.2 Internal Ballistic Design

To design a propulsion system, first, operational constraints should be defined. Usually, a payload mass and a ΔV requirement are given for a system to deliver a specific payload to its target orbit. Furthermore, secondary requirements such as volumetric envelope, maximum acceleration for structural reasons and burn time limitations to avoid grain cooking may be established. Since the purpose of this thesis is to show the advantage of electric pump-fed system with a specifically designed pump on a specific system, these requirements are omitted and a total impulse target along with and fixed oxidizer mass flow rate are chosen as more convenient parameters. In that regard, systems are compared according to their ΔV capability.

To start the design calculations, an average O/F is chosen and delivered I_{sp} is guessed for the system to calculate the mass of the propellants to achieve target total impulse. The relation comes from the time integration of thrust.

$$I_{tot} = \int_0^{t_b} T \mathrm{d}t = \int_0^{t_b} \dot{m}_{tot} I_{sp}\ g_0\ \mathrm{d}t = \int_0^{t_b} \dot{M}_p I_{sp}\ g_0\ \mathrm{d}t \tag{4.37}$$

Noting that $\dot{m}_{tot}$ is the total propellant mass flow rate through the nozzle is scalarly negative of the rate of change in propellant mass M_p on board.

$$M_p = \frac{I_{tot}}{g\ I_{sp,del}} \tag{4.38}$$

Delivered I_{sp} is defined as the time average of I_{sp} over the burn time.

$$I_{sp,del} = \frac{\int_0^{t_b} I_{sp} \mathrm{d}t}{t_b} \tag{4.39}$$

After calculating total propellant mass, fuel and oxidizer mass are approximated separately by using the average O/F.

$$M_{ox} = \frac{O/F_{ave}}{1 + O/F_{ave}} M_p \tag{4.40}$$

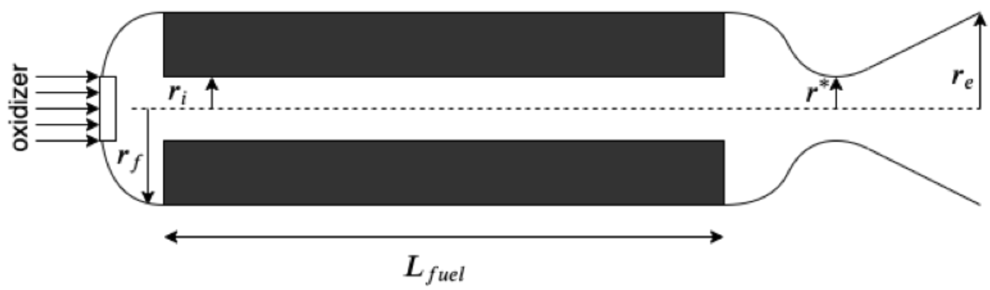

Figure 4.6: Hybrid rocket motor cross section example.

$$M_{fuel} = \frac{1}{1 + O/F_{ave}} M_p \tag{4.41}$$

Total oxidizer mass is used to calculate the burn time with chosen oxidizer mass flow rate.

$$t_b = \frac{M_{ox}}{\dot{m}_{ox}} \tag{4.42}$$

Burn time is used for the finding initial and final port diameter of the fuel. ODE presented in equation 4.35 is rearranged as below.

$$\frac{\mathrm{d}r}{\mathrm{d}t} = a\left(\frac{\dot{m}_{ox}}{\pi r^2}\right)^n \tag{4.43}$$

$$\int_{r_i}^{r_f} \mathrm{d}r\ \pi^n\ r^{2n} = \int_0^{t_b} a\dot{m}_{ox}^n\ \mathrm{d}t \tag{4.44}$$

Integrating both sides yields

$$\pi^n \left(\frac{r_f^{2n+1}}{2n+1} - \frac{r_i^{2n+1}}{2n+1}\right) = a\dot{m}_{ox}^n\ t_b \tag{4.45}$$

At this point, deciding the a final to initial port diameter ratio would determine the initial and final port diameter. This value is taken as 2 ($r_f/r_i = 2$) because larger values usually result in grain cracking in fuel casting process and lower values would result in low volumetric loading.

$$r_i = \left(\frac{(2n+1)a\dot{m}_{ox}^n\ t_b}{\pi^n\ (2^{2n+1} - 1)}\right)^{\frac{1}{2n+1}} \tag{4.46}$$

$$r_f = 2\left(\frac{(2n+1)a\dot{m}_{ox}^n\ t_b}{\pi^n\ (2^{2n+1} - 1)}\right)^{\frac{1}{2n+1}} \tag{4.47}$$

Using the fuel mass and port diameters, grain length is obtained according 4.48.

$$L_{fuel} = \frac{M_{fuel}}{\rho_{fuel}\ \pi(r_f^2 - r_i^2)} \tag{4.48}$$

Once the grain parameters are approximated (See Figure 4.6, o more accurate internal ballistic code is run with time discretization on regression rate.

At the first time step, constants oxidizer mass flow rate is used to calculate the instantaneous fuel regression rate by using Equation 4.43.

This instantaneous value is used to calculate the instantaneous rate of fuel mass consumption and instantaneous O/F.

$$\dot{m}_{fuel} = \rho_{fuel} 2\pi\ r L_{fuel} \dot{r} \tag{4.49}$$

With the calculated value' initial nozzle throat diameter can be found by using the relation 4.33. Combustion efficiency η_c is assumed as 0.95 and nozzle coefficient of discharge C_d is assumed as 0.99 for non-ideal combustion and non-inviscid nozzle flow.

$$A^{*t=0} = \frac{\dot{m}_{tot}^{t=0} c^{*t=0} \eta_c}{p_{ch}^{t=0} C_d} \tag{4.50}$$

where $\dot{m}_{tot} = \dot{m}_{ox} + \dot{m}_{fuel}$.

$$r^{*t=0} = \sqrt{\frac{A^{*t=0}}{\pi}} \tag{4.51}$$

For good vacuum performance an initial area ratio of 50 is chosen for the divergent part of the nozzle. This ratio is updated as the nozzle throat enlarges due to erosion. It is also assumed that no erosion takes place at the nozzle exit.

$$AR^t = \frac{A_e}{A^{*t}} \tag{4.52}$$

At this point, known parameters p_{ch}, O/F and AR are used to calculate I_{sp} via NASA CEA and instantaneous thrust is found. Nozzle efficiency due to 3D flow loses is assumed as 0.97.

$$T^t = \dot{m}_{tot}^t I_{sp}^t g_0 \eta_c \eta_{nozzle} \tag{4.53}$$

At the end of the time step port diameter, nozzle throat diameter and combustion chamber pressure are updated to be used in the next time step. Euler explicit method is used for time marching. Nozzle throat erosion rate is similarly calculated with a nozzle erosion model. Coefficients for erosion model are assumed from a case having a 50 bar of combustion pressure and 0.005 cm/s of nozzle erosion rate.

$$\dot{r}^* = a_n G_m^n \tag{4.54}$$

where $G_m = \dot{m}_{tot}/A^*$

$$r^{*t+1} = r^{*t} - \dot{r}^* \Delta t \tag{4.55}$$

$$r^{*t+1} = r^{*t}\_\dot{r}^{*t} \Delta t \tag{4.56}$$

$$p_{ch}^{t+1} = \frac{\dot{m}_{tot}^t c^{*t} \eta_c}{A_{throat}^t C_d} \tag{4.57}$$

This procedure is progressed over time from $t = 0$ to $t = t_b$. At the end of iterations, instantaneous thrust is numerically integrated to find total impulse and $I_{sp,del}$ is updated accordingly accordingly.

$$I_{tot} = \sum_{t=0}^{t=t_b} T^t \Delta t \tag{4.58}$$

$$I_{sp,del} = \frac{I_{tot}}{M_p g_0} \tag{4.59}$$

Then all of the calculations explained above is repeated with updated $I_{sp,del}$ until $|I_{tot} - I_{tot,req}| < 200\ Ns$.

4.2.3 Nozzle Design

For simplicity, a nozzle with 15° conical divergent section is considered. Although conical nozzles tend to be longer and heavier, the adverse mass effect is introduced to both systems equally so it would not add any bias to the analysis. Calculated nozzle exit diameter and throat diameter from internal ballistic code are used to calculate geometrical parameters of the nozzle assembly. Nozzle is considered as ablative layer wrapped with a metal nozzle jacket.

Layers' thicknesses are calculated at the throat and exit section and with a linear transition assumption. Layer thickness of ablative layer is found from the nozzle erosion amount at the throat and a given exit thickness of 1 mm. At the throat, ablative layer thickness is increased by a factor of 1.1 to ensure the presence of ablative layer to protect nozzle jacket towards end of the burn. This margin is included in equations 4.61, 4.62 and 4.66.

Static pressures at the throat and nozzle exit are found by the isentropic flow condition in the nozzle.

$$\frac{1}{AR^{t=0}} = \left(\frac{\gamma+1}{2}\right)^{\frac{1}{\gamma-1}} \left(\frac{p_e}{p_{ch}}\right)^{\frac{1}{\gamma}} \left[\left(\frac{\gamma+1}{\gamma-1}\right)\left(1-\frac{p_e}{p_{ch}}^{\frac{\gamma-1}{\gamma}}\right)\right]^{1/2} \tag{4.60}$$

When $AR = 1$, p_e value is the static pressure at the throat, p^*. It is assumed that the nozzle jacket would endure the entire interior pressure so the wall thicknesses are calculated at the throat and nozzle exit. A safety factor k_s of 1.3 is taken for the thickness calculations of nozzle jacket and a minimum gauge thickness of 2 mm is taken for manufacturing purposes.

$$t^*_{wall,j} = \frac{k_s\ p^*(1.1\ r^*_f)}{\sigma_{y,j}} \tag{4.61}$$

$$t^e_{wall,j} = \frac{k_s p_e r_e}{\sigma_{y,j}} \tag{4.62}$$

To find nozzle mass, nozzle length is found to integrate the area over length.

$$L_{nozzle} = \frac{r_e - r^*_i}{tan(15)} \tag{4.63}$$

Then the integration of dA over L gives the volume of layers.

$$V_{layer} = \int_0^L dA_{layer} dx \tag{4.64}$$

where

$$dA_{ab} = [1.1 r^*_f + ((r_e + t^e_{ab} - r^*_f)/L)x]^2 - [r^*_i + ((r_e - r^*_i)/L)x]^2 \tag{4.65}$$

$$dA_j = [(1.1r_f^* + t_j^* + ((r_e + t_{ab}^e + t_j^e - r_f^* - t_j^*)/L) * x]^2 - [r_f^* + ((r_e + t_{ab}^e - r_f^*)/L) * x]^2 \quad (4.66)$$

Definitions of the terms are also illustrated in Figure 4.7. Mass of the layer are found with respect to their material density.

$$M_{layer} = V_{layer}\rho_{layer} \quad (4.67)$$

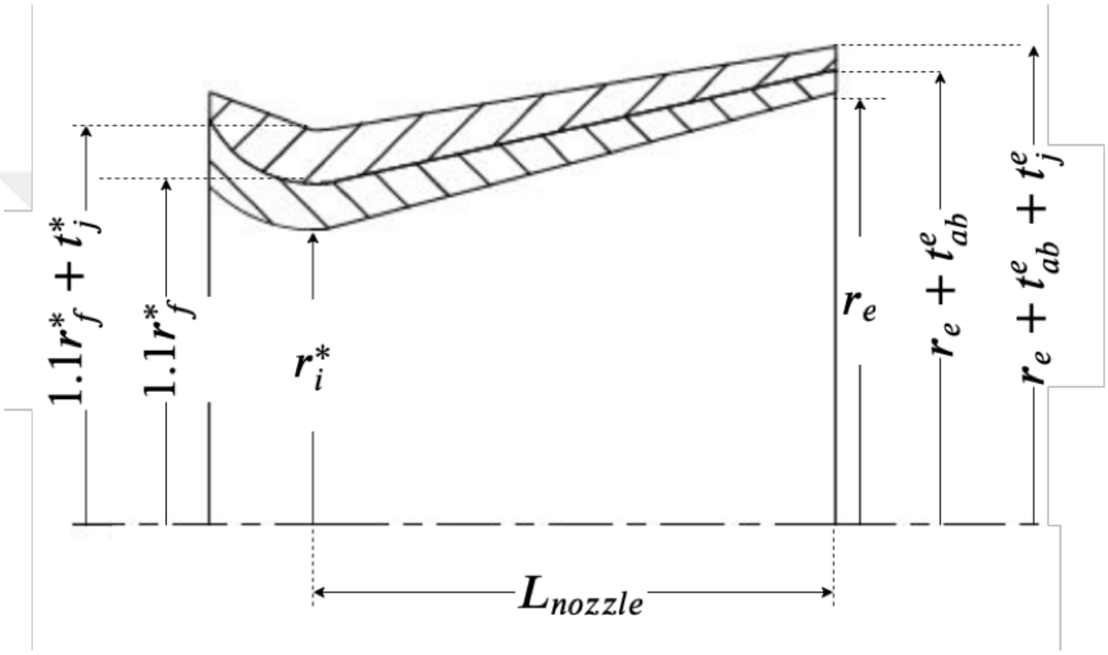

Figure 4.7: Nozzle cross section.

4.3 Propellant Feed System Design

After determining the rocket motor size, and propellant mass, a feed system design can be made. For this procedure, the required oxidizer tank volume is used to calculate the amount of pressurization gas. This procedure is applied also for the electric pump-fed system since the pump requires oxidizer tank to be at a certain pressure level as well. Pressurization gas is chosen to be helium.

4.3.1 Pressurization System Design

Pressurization of the oxidizer tank is achieved by using a pressurization gas stored in a high-pressure tank. The amount of the pressurization gas needed to keep the oxidizer tank at a certain pressure can be found by employing an ideal gas assumption.

Oxidizer tank volume is found by calculating the total oxidizer volume and including an ullage factor of 1.05.

$$V_{oxtank} = 1.05\frac{M_{ox}}{\rho_{ox}} \tag{4.68}$$

$$M_{pg} = \frac{p_{oxtank}(V_{oxtank} + V_{presstank})}{R\,T_{pg,f}} \tag{4.69}$$

It is assumes that at the end of the burn both tanks are at the same pressure and temperature, neglecting the heat transfer between the cryogenic liquid oxidizer and initial ullage gas mass.

The expansion process of helium from the initial pressurization tank pressure to oxidizer tank operating pressure is thought to be a polytropic process. The polytropic coefficient n is assumed as 1.2 in calculations. With a determined initial pressurization tank pressure, pressurization tank volume can be found by Equation 4.70.

$$\frac{p_{presstank,i}}{p_{oxtank}} = \left(\frac{V_{presstank} + V_{oxtank}}{V_{presstank}}\right)^{n} \tag{4.70}$$

Then $T_{pg,f}$ can be found with given $T_{pg,i}$.

$$\frac{T_{pg,f}}{T_{pg,i}} = \left(\frac{V_{presstank}}{V_{presstank} + V_{oxtank}}\right)^{n-1} \tag{4.71}$$

4.3.2 Tank Design

Tanks need to be designed to withhold their operating pressure with a safety margin. Before determining the wall thickness of the tank, first, its geometry is decided. For the packaging requirements, the maximum diameters of tanks are matched to nozzle diameter. If a spherical tank geometry with a diameter equal or lower than 105 % of nozzle diameter is viable, this geometry is pursued. Otherwise, a cylindrical geometry with semi-ellipsoidal ends for oxidizer tank and a cylindrical geometry with hemispherical end for pressurization tank are pursued. To determine tank wall thickness a stress calculation is done.

For tank ends the minimum wall thickness is calculated.

$$t_{wall} = k_s K \frac{p\ r}{2\sigma_y} \tag{4.72}$$

Where K is the stress concentration factor around changes in the curvature of the surface geometry. For ellipsoidal ends, K is defined on semi-major axis a and semi-minor axis b.

$$K = [2 + (a/b)^2]/3 \tag{4.73}$$

For hemispherical s geometries $K = 1,\ (a = b)$.

In the case of cylindrical tanks where meridional stresses on the barrel of the tank are higher than hoop stresses, wall thickness should be determined with meridional stress in cylindrical sections.

$$t_{wall} = k_s \frac{p\ r}{\sigma_y} \tag{4.74}$$

For a cylindrical tank with 2:1 ellipsoidal ends, the wall thickness calculations match since $K = 2$. A minimum gauge thickness is considered to prevent possible buckling of the tanks under compression.

Surface area is calculated according to tank volume and shape. For spherical tanks surface is found by

$$S_{tank} = 4\pi\ r^2 \tag{4.75}$$

For cylindrical geometry with hemispherical ends, surface are of the domes are calculated as the same and cylindrical side wall surface is added.

$$S_{tank} = 2\pi r L + 4\pi r^2 \tag{4.76}$$

where

$$L = \frac{V - \frac{4}{3}\pi r^3}{\pi r^2} \tag{4.77}$$

For cylindrical geometry with ellipsoidal ends the expression becomes

$$S_{tank} = 2\pi r\ L + 4\pi \left(\frac{(r^2)^{1.6} + 2(\frac{r^2}{2})^{1.6}}{3} \right)^{1/1.6} \tag{4.78}$$

where

$$L = \frac{V - \frac{4}{3}\pi r^2 \frac{r}{2}}{\pi r^2} \tag{4.79}$$

Tank mass is calculated with the obtained, surface area, wall thickness and material properties.

$$M_{tank} = \rho_{material} S_{tank} t_{wall} \tag{4.80}$$

4.4 Pump Drive System Design

Pump drive system is the system that provides the required power to the pump at the required speed and torque for the entire operation time. The proposed system considered in this thesis uses electric motors powered by battery as the energy source and controlled by an electronic speed controller as the control unit. In flight systems, these components are specifically tailored for the system to achieve high power to mass ratio which is critical for system performance. Ideally, these components are designed for operational constraints set by the pump, since the design and development of these components are research topics individually by themselves (as in [Dlugiewicz et al., 2012]), the following design procedure is based on the off-the-shelf component data. Since these components' power and energy levels are not exactly the same as the system requirements, two additional parameters are introduced for scaling purposes. Power density(δ) is the ratio of the rated power of the component to its mass with a unit of kW/kg and energy density, used for batteries, is the ratio of available energy stored in the components to its mass with a unit of Wh/kg. This strategy yields a more conservative mass calculation since power density and energy density of industry-standard components are significantly lower than aerospace-grade components with flight-weight design.

4.4.1 Electric Motor Selection and Sizing

Centrifugal pumps in the industry generally use asynchronous AC motors powered by tri-phase 380/400 V electric source. But for high power density applications, these industry-standard motors do not meet the requirements of weight and efficiency. Duffy, compares different types of electric motor according to their suitability of hybrid electric or turbo-electric propulsion. The author, suggests permanent magnet synchronous motor (PMSM) over induction motors and synchronous reluctance motors for high power density applications [Duffy, 2015].

For high power and high-speed applications, motor cooling can be a difficult challenge. But electric motors used in cryogenic applications benefit from the low temperatures [Liping Zheng et al., 2005] and this working condition also enables motor components to be smaller in size, therefore increases power density [Guo et al., 2018].

A PMSM motor is considered for this system and to anticipate the mass of the motor, a literature survey is conducted. Density values gathered from literature and used in similar research are presented in Table 4.1.

Table 4.1: Electric motor data.

Source	Power Density (kW/kg)	Efficiency
[Rachov et al., 2013]	3.8	0.8
[Duffy, 2015]	5.8	0.96
[Gegeoglu et al., 2019]	5	0.95

In line with the previous research, a power density value of 5kW/kg and an efficiency value of 0.95 are adopted.

Motor mass is calculated according to the required power by the pump.

$$P_{em} = \frac{P_{pump}}{\eta_{pump}} \tag{4.81}$$

where $P_{pump} = Q\rho g_0 \Delta H$ is the hydraulic power used for pressurizing propellant and η_{pump} is the hydraulic efficiency of the pump. Electric motor mass is estimated with the accepted power density δ_{em} .

$$M_{em} = \frac{P_{em}}{\delta_{em}} \tag{4.82}$$

4.4.2 Electronic Speed Controller Selection and Sizing

Electric motor requires commutation to generate motion therefore an electronic speed controller(ESC) is required to control the motor. Electronic speed controller takes DC current from batteries and inverts them to switching current in motor phases. Although this component does not substantially contribute to system mass, it is still necessary to take ESC mass into account for accuracy of the analysis. ESC power density and efficiency are taken from previous research as 60 kW/kg and 0.85 [Rachov et al., 2013]. Mass of the ESC is calculated based on the required power by the motor.

$$P_{ESC} = \frac{P_{em}}{\eta_{em}} \tag{4.83}$$

$$M_{ESC} = \frac{P_{ESC}}{\delta_{ESC}} \tag{4.84}$$

4.4.3 Battery Selection and Sizing

To power the electric motor, Li-Po, Li-Ion and Li-S battery types are considered. The selection of the battery type comes from application itself. While Li-Po batteries are advantageous in power intensive applications, Li-Ion and Li-S batteries are more suitable for energy intensive applications. Power and energy density from the previous research is presented in Table 4.2. Li-Ion and Li-S battery properties are taken from

Table 4.2: Battery data.

Source	Type	Power Density (kW/kg)	Energy Density (Wh/kg)
[Kwak et al., 2018]	Li-Po	6.95	195
[Rachov et al., 2013]	Li-Ion	2	220
[Rachov et al., 2013]	Li-S	1.25	350

Battery mass is calculated based on the required power and required energy. The required power of the battery is estimated from the ESC specifications and battery mass based on power requirements is estimated with the accepted power density $\delta_{bat,P}$.

$$P_{bat} = \frac{P_{ESC}}{\eta_{ESC}} \tag{4.85}$$

$$M_{bat,P} = \frac{P_{bat}}{\delta_{bat,P}} \tag{4.86}$$

Total available energy requirement of the battery is calculated with required power and operation time.

$$\eta_{bat,E} E_{bat} = \frac{P_{ESC}}{\eta_{ESC}} t_b \tag{4.87}$$

Efficiency for the battery energy is introduced since discharge time effects the available energy in the battery cell. For this value an empirical correlation presented by Kwak is used [Kwak et al., 2018].

$$\eta_{bat,E} = 0.093 ln(t_b) + 0.3301 \tag{4.88}$$

Mass estimation of the battery based on energy requirements is consequently made with the accepted energy density $\delta_{bat,E}$.

$$M_{bat,E} = \frac{E_{bat}}{\delta_{bat,E}} \tag{4.89}$$

Depending on the application, the process is either power intensive or energy intensive so the battery should be designed with the limiting factor. Therefore maximum of two mass estimation is taken for the design.

$$M_{bat} = \max(M_{bat,E}, M_{bat,P}) \tag{4.90}$$

Chapter 5

SYSTEM DESIGN

For a comprehensive analysis to reveal the advantage of the proposed approach, an example propulsion system that is suitable for an upper stage mission is designed. The propulsion system is decided to deliver 1 MNs of total impulse. Also, 20 bar of combustion chamber pressure for the hybrid rocket motor is selected. For optimum operation, the oxidizer flow rate is set for the B.E.P of the pump.

5.1 Pump Design

5.1.1 Pump Hydraulic Design

As it will be discussed later in this chapter, pump specific speed of the validated model is used for preliminary design of the pump. Therefore specific speed value of 648 (in Imperial units with rpm, ft, gpm) and 12.75 (in SI units with rpm,m,m^3/s) is adopted for design. 30 bar of differential head is chosen.This yields at least 10 bar of injector ΔP. Liquid to be pumped is chosen as LOX at 95 K. For the motor speed, 12 000 rpm of shaft speed is chosen. $H = 273$ m $Q = 5.12$ l/s $N = 12000$ rpm

Differential head is found as 273 m with the density of LOX at 95 K.

$$H = \frac{30 \times 10^5 (\mathrm{Pa})}{1116.9(\mathrm{kg/m^3})\ 9.81(\mathrm{m/s^2})} \tag{5.1}$$

Then from the specific speed formula, design flow rate is found as 5.12 l/s.

$$12.75 = \frac{12000\sqrt{Q}}{H^{3/4}} \tag{5.2}$$

With these inputs, main dimensions of the impeller and the volute are found with the procedures suggested by Gulich and Stepanoff (See Table 5.1).

Table 5.1: Pump main dimensions with design methods.

Parameter	Symbol	Stepanoff	Gulich
Impeller Dia.	D_2	109.6	111.4
Impeller Inlet Dia.	D_1	35.1	34.2
Outlet Blade Angle	β_2	22.5	22.5
Inlet Blade Angle	β_1	20.4	22.95
Outlet Blade Width	b_2	4.4	5.5
Inlet Blade Width	b_1	7.6	9.7
Volute Base Circle Dia.	D_3	116.8	120.7
Volute width	b_3	13.1	16.4
Volute throat height	a_3	11.6	8.5
Volute cut water angle	α_{3B}	5.3	4.3
Volute Cutwater Thickness	e_3	2	2

A CFD model is created with the calculated parameters and the solution indicated a larger head value than intended. This is thought to be related to the disparity between the speed regimes of our pump and industrial pump data used to derive the empirical correlations. Most of the pumps used in pump statistics are industrial pumps rotating around 3000 rpm. For speeds at the level of 12000 rpm, these empirical correlations are unlikely to produce accurate results.

Therefore, the design parameters are iterated until the desired head level is obtained. This iteration is terminated when the head value of 282 m is reached instead of the design level of 273 m. This is done deliberately to account for additional flow loss in actual geometry. Hydraulic efficiency is found to be 0.87 but this value the efficiency is taken as 0.7 to account for additional flow and mechanical losses. Model parameters at the end of the iteration process are presented in Table 5.2.

Table 5.2: Pump main dimensions resulted in CFD iterations.

Parameter	Symbol	Value
Impeller Dia.	D_2	103
Impeller Inlet Dia.	D_1	40
Outlet Blade Angle	β_2	22.5
Inlet Blade Angle	β_1	19
Outlet Blade Width	b_2	5
Inlet Blade Width	b_1	7.5
Volute Base Circle Dia.	D_3	107
Volute width	b_3	16
Volute throat height	a_3	11.6
Volute cut water angle	α_{3B}	5
Volute Cutwater Thickness	e_3	2

5.1.2 Pump Mechanical Design

Mechanical design of the pump is done in CAD environment (See Figures 5.1, 5.2 and 5.3) . The solid model includes impeller, volute, shaft and sealing elements with assigned material data.

The mass of the pump system components other than the pump itself is estimated from the literature data while the pump is modeled in CAD environment to acquire high fidelity mass estimation.

Figure 5.1: Pump CAD model front view.

Figure 5.2: Pump CAD model orthogonal view.

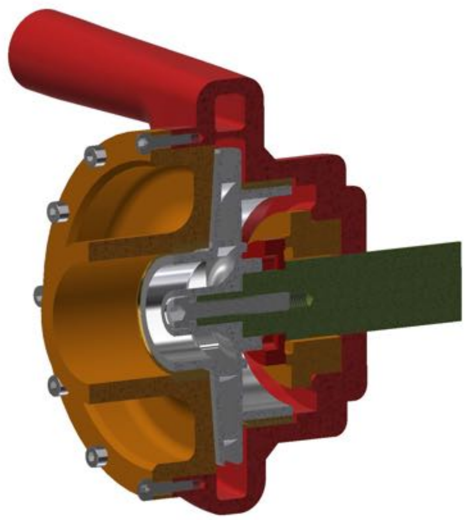

Figure 5.3: Cross section of the pump.

Pump materials are chosen in consideration for LOX compatibility, combining cryogenic performance with spark resistance. In conclusion, pump shaft and the casing is decided to be manufactured from AISI 304L Stainless Steel while the impeller and labyrinth seal material is chosen as Inconel 625. The selection of AISI 304L rather than AISI 316L is because of its better machining properties and the selection of Inconel 625 is because of the ignition resistance due to possible particle impact.

Sealing is a critical issue for rotating machinery especially in cryogenic temperatures. Since the matter deserves its own research focused on sealing, the details of the design is omitted from the scope of this thesis. Nevertheless the mechanical seal is thought to be the main sealing mechanism of the shaft which prevents leakage outside of the system. Internal leakage from downstream of the impeller to its upstream will be minimized with annular seal which consist t cylindrical surfaces running with small clearances. Bolts are chosen as stainless steel A2 quality and the total assembly mass is calculated by the CAD software as 4.5 kg.

It should be noted that the wall thickness of the volute casing is modeled for thicker than the requirement to withstand the internal pressure. The notion of this behavior is because of the weld operation planned for volute manufacturing since casting method is too expensive for prototype production. Nevertheless, pump mass obtained from CAD is multiplied with 1.3 to account for any possible interface or gearbox assembly.

$$M_{pump} = 5.85\ kg \tag{5.3}$$

5.1.3 Pump Drive System

Electric pump drive system components are sized according to Section 4.4 and listed in Table 5.3.

Table 5.3: Pump drive system mass estimation.

Parameter	Symbol	Value
Hydraulic Power	P_h	15.33 kW
Electric Motor Power	P_{em}	21.9 kW
Electric Motor Mass	M_{em}	4.38 kg
ESC Output Power	P_{ESC}	23.05 kW
ESC Mass	M_{ESC}	0.38 kg
Battery Power	P_{bat}	24.26 kW
Battery Energy	E_{bat}	445.38 Wh
Battery Mass, LiPo	M_{bat}	3.90 kg
Battery Mass, Li-on	M_{bat}	13.56 kg
Battery Mass, Li-S	M_{bat}	21.69 kg

The power intensive nature of the application is evident from the battery mass estimation, therefore Li-Po batteries are considered for the system.

The total pump system mass is estimated as 14.51 kg from the calculations above. This value however is increased by a factor of 1.2 to account for battery and ESC casing, possible electric motor cooling system and battery thermal management components.

$$M_{sys,pump} = 17.41 \text{ kg} \tag{5.4}$$

5.2 Rocket Motor Design

With the selected oxidizer flow rate and the total impulse objective of 1 MNs, an internal ballistic design can be made by following the procedure in Section 4.2 .

For the propellant combination of LOX/Paraffin, regression rate coefficients and approximate delivered I_{sp} with predicted average O/F are presented in Table 5.4.

Table 5.4: Parameters and coefficients used in internal ballistic code.

Parameter	Symbol	Value	Reference
Regression Rate Coefficient	a	0.0488	[Karabeyoglu et al., 2004]
Regression Rate Exponent	n	0.62	[Karabeyoglu et al., 2004]
Nozzle Erosion Coefficient	a_n	1.5×10^{-5}	
Nozzle Erosion Exponent	m	1	
Predicted delivered I_{sp}	$I_{sp,del}$	330	
Initial Average O/F	$O/F_{avg,i}$	2.7	
Initial Chamber Pressure	$p_{ch,i}$	20 bar	
Oxidizer Mass Flow Rate	$\dot{m}_{ox}$	5.718 kg/s	
Port diameter ratio	r_f/r_i	2	
LOX Density	ρ_{ox}	1116.9 kg/m^3	
Paraffin Density	ρ_{fuel}	930 kg/m^3	

Regression and erosion rate coefficients are presented with rate units of cm/s and flux units of kg/cm^{2}s.

5.2.1 Internal Ballistic Design and Chamber Mass Estimation

With the selected parameters in Table 5.4 a propulsion system design for an upper stage motor is made and resulted design parameters are listed in Table 5.5. Dry mass of the combustion chamber is also calculated by considering the combustion chamber as a pressure vessel with working pressure. A 2:1 ellipsoidal geometry is selected for the end sections of the combustion chamber. Wall thickness and surface area are found according to equations 4.72 and 4.78.

Table 5.5: Output parameters of internal ballistic code and chamber mass estimation.

Parameter	Symbol	Value
Burn Time	t_b	40.22 s
Oxidizer Mass	M_{ox}	230 kg
Fuel Mass	M_f	85.19 kg
Average O/F	O/F_{avg}	2.7
Delivered specific impulse	$I_{sp,del}$	323.40 s
Grain Diamater	D_f	34.20 cm
Grain Length	L_f	131.37 cm
Combustion Chamber Dry Mass	M_{ch}	61.69 kg

5.2.2 Nozzle Mass Estimation

Nozzle mass is calculated with procedures explained in section 4.2.3. For the nozzle jacket steel alloy 4130 and for the ablative layer silica phenolic are chosen as materials. Silica phenolic material is chosen o be FM5020 from the reference [Williams and Curry, 1992].

Table 5.6: Nozzle assembly mass estimation.

Parameter	Ablative Layer	Nozzle Jacket
Material	Silica Phenolic	AISI 4130[1]
Density, kg/m^3	1709	7850
Yield Strength, MPa	-	435
Layer Mass, kg	10.7	20.66

Layer mass obtained in Table 5.6 only includes the divergent section of the nozzle. To include the convergent section and assembly interface, the total layer mass is multiplied by 1.1 to estimate entire nozzle mass.

$$M_{nozzle} = 34.5 \text{ kg} \tag{5.5}$$

5.3 Pressurization and Feed System Design

Pressurization and feed system are designed for the pressure-fed system and electric pump-fed system separately since the operating pressure of the oxidizer tank is different. To reduce the possibility of a gas phase flow, oxidizer mass is taken as 250 kg rather than 230 kg to leave some liquid margin. Resulting values are presented in Table 5.8. For oxidizer tank Aluminum alloy 2219-T87 is chosen for its cryogenic performance and LOX compatibility, for pressurization tank Steel alloy 4130 is chosen due to its good weldability. Tank material properties are presented in Table 5.7.

Table 5.7: Materials used for tanks.

Material	Density, kg/m^3	Yield Strength, MPa
AISI 4130[1]	7850	435
2219-T87[2]	2840	393

[1]Mechanical properties have been accessed on 25.02.2020 at: http://asm.matweb.com/search/SpecificMaterial.asp?bassnum=m4130r,

Table 5.8: Pressurization system specifications.

Parameter	Symbol	Press-Fed	Electric Pump-Fed
Polytropic Gas Coefficient	n	1.2	1.2
Initial Press. Tank Pressure	$p_{presstank,i}$	300 bar	300 bar
Initial Press. Tank Temperature	$T_{pg,i}$	280 K	280 K
Press. Tank Volume	$V_{presstank}$	53.9 liter	14.7 liter
Press. Gas Mass	M_{pg}	2.78 kg	0.76 kg
Press. Tank Geometry		Spherical	Spherical
Press. Tank Mass	$M_{tank,p}$	56.90 kg	15.49 kg
Secondary Component Mass	M_{other}	10 kg	10 kg
Total Press. System Mass	$M_{sys,p}$	69.68 kg	26.25 kg
Oxidizer Tank Volume	V_{oxtank}	235 liter	235 liter
Oxidizer Tank Geometry		CEE	CEE
Oxidizer Tank Pressure	p_{oxtank}	40 bar	10 bar
Oxidizer Tank Mass	$M_{tank,ox}$	50.05 kg	13.97 kg

As it can be seen from Table 5.8 there is substantial pressurization tank mass difference between the systems. This is because of both increased pressurization tank volume and increase in wall thickness due to tank diameter. It should also be noted that oxidizer tank wall thickness for electric pump-fed system hit the minimum gauge thickness 2 mm although it can be about 1.8 mm to withhold the pressure.

[1]Mechanical properties have been accessed on 25.02.2020 at:
http://asm.matweb.com/search/SpecificMaterial.asp?bassnum=m4130r.

[2]Mechanical properties have been accessed on 25.02.2020 at:
http:/http://asm.matweb.com/search/SpecificMaterial.asp?bassnum=MA2219T87.

Chapter 6

CFD ANALYSIS

Due to complex geometries of hydraulic components of the pump, the main dimensions obtained from 1-D analysis are not sufficient to verify the performance of the pump. Therefore a numerical analysis is required to be executed on the fluid domain of the pump. For this purpose, ANSYS Workbench is used to model the geometry and run a computational fluid dynamics analysis (with CFX solver).

6.1 Geometry

The main dimensions obtained from the previous section are used to create a 3D model of the impeller and volute.

Impeller geometry is created by using BladeGen module in ANSYS Workbench (See Figure 6.1). In order to reduce slip, splitter blades were added to the design.

Apart from the main dimensions, there are few parameters that need to be determined by the designer. These parameters contribute to the 3D geometry of the blades and they can not be exactly determined from the 1-dimensional analytical method that is introduced in Chapter 4. These parameters are then chosen from the examples of pumps that are already in use and from the recommendations by [Stepanoff, 1957] and [Gülich, 2010].

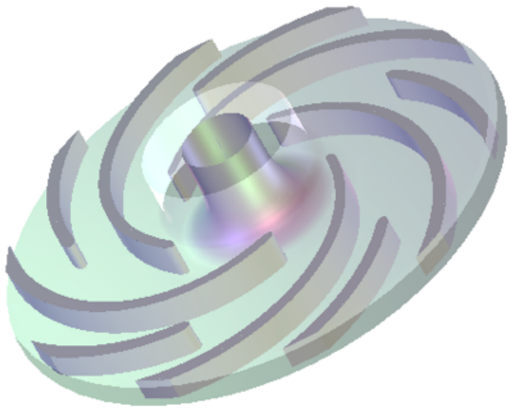

Figure 6.1: Model of the impeller(with transparent shroud).

Volute geometry is created in a 3D CAD modeling software with the cross-section of the volute in plan view and extruded along the axis of rotation. Sidewall gaps in front and back of the impeller are also accounted for while building the fluid domain of the volute (See Figure 6.2).

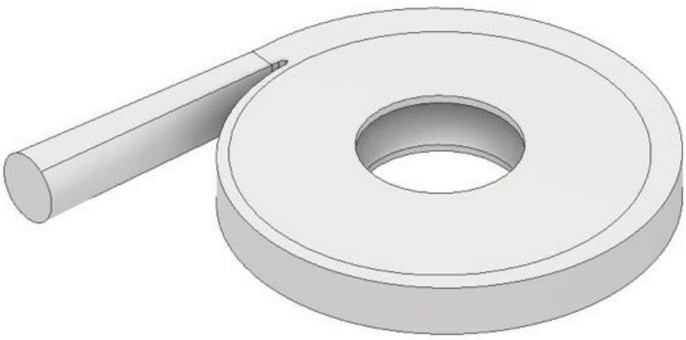

Figure 6.2: Fluid domain of the volute.

6.2 Meshing

After geometries representing the fluid domain are obtained by the mentioned techniques in the previous section, these geometries are discretized by meshing algorithms.

Blade passage design in BladeGen is transferred to TurboGrid module to create a structured mesh (See Figure 6.3). The program automatically recognized the hub, shroud and blade geometries and create a mesh with the selected mesh options consisting, mesh size and boundary layer refinement options. Boundary layer reso-

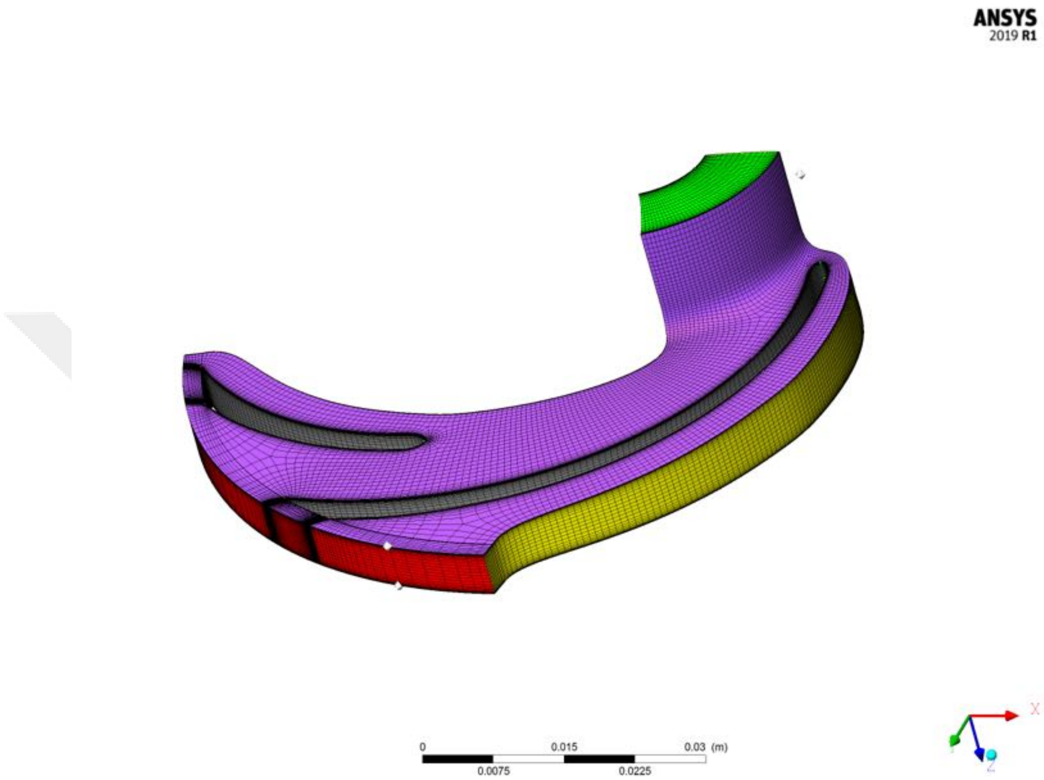

Figure 6.3: Mesh of the impeller passage.

lution is determined with the inflation properties of the mesh near walls (See Figure 6.4). A value around 0.02 mm as the first layer thickness and growth rate of 1.3 is chosen although other values were also tried in CFD and no significant difference in engineering values were seen.

Volute is modeled in a separate CAD program and is meshed under the Meshing Cell of ANSYS Workbench (See Figure 6.5). After the model is imported to the geometry section of the cell, the geometry is edited in SpaceClaim. This is suggested for complex geometries since unimportant details such as fillets, chamfers, and small gaps make meshing problematic and also causes errors in the solution. It is also useful to create interface surfaces where to surfaces to be interfaced are coinciding but are not of the same size. A surface split operation is then executed to define an

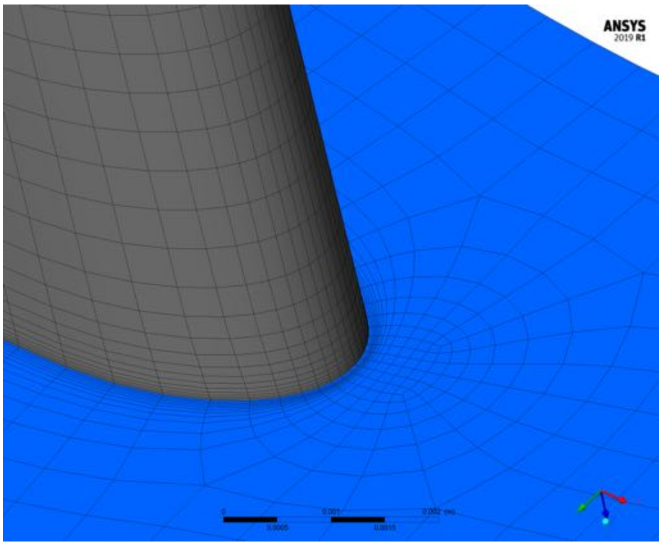

Figure 6.4: Mesh inflation for boundary layer resolution around blade tip.

interface region between the impeller outlet surface and the volute inlet surface.

Figure 6.5: Volute mesh.

Mesh dependency of the model is checked with different number of mesh cells and a minor difference in engineering value head is observed as presented in Figure 6.6. Nevertheless, mesh number of 6 million is chosen for the rest of the analysis.

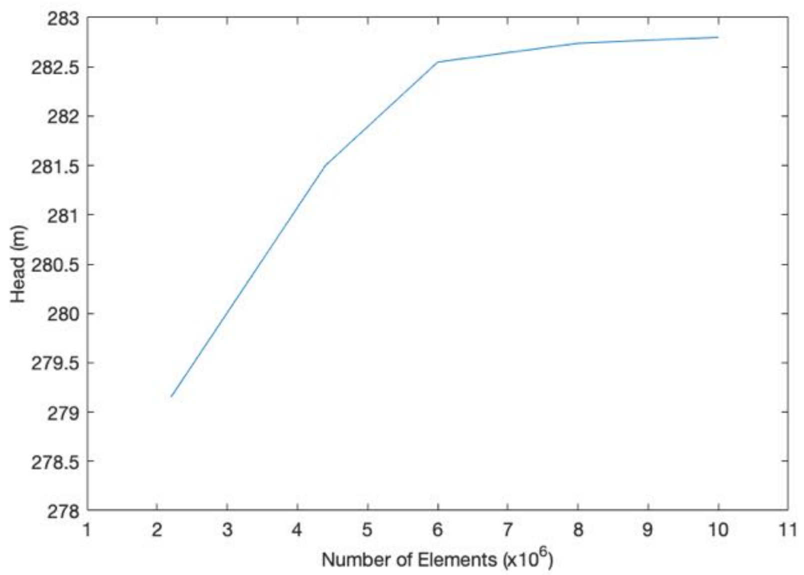

Figure 6.6: Mesh dependency of the model.

6.3 CFD Model

After meshing is completed, mesh files are imported to the CFX module in ANSYS Workbench. In CFX cell, first, CFX-Pre is used to set up the model. In the model, multiple reference frame(MRF) method is used for rotating and stationary domains. The following Reynold Averaged Navier Stokes(RANS) equations are solved with a finite volume(FV) approach.

6.3.1 Governing Equations

For the numerical flow simulation, incompressible Navier-Stokes equations are solved for the entire domain.

$$Continuity : \nabla \cdot \overrightarrow{U} = 0 \tag{6.1}$$

$$Momentum : \rho \frac{D\overrightarrow{U}}{Dt} = -\nabla p + \mu_{eff} \nabla^2 \overrightarrow{U} + \overrightarrow{F} \tag{6.2}$$

The external force $\overrightarrow{F}$ accounts for buoyancy, coriolis and centrifugal forces. Buoyancy forces are excluded from the calculations since the magnitude is neglibily small. And coriolis and centrifugal force terms are added to the equations for the rotating domain where external force term is used for stationary domain.

$$\overrightarrow{F} = -\rho[\overrightarrow{\Omega} \times (\overrightarrow{\Omega} \times \overrightarrow{r}) + 2\overrightarrow{\Omega} \times \overrightarrow{U}] \tag{6.3}$$

In equation 6.3, $\overrightarrow{\Omega}$ stands for the rotational velocity vector and $\overrightarrow{r}$ stands for the location vector.

For turbulence models, standard k-ϵ , standard k-ω and SST k-ω models are considered. Gülich gives an overview of those 3 models, and while he argues that standard k-ϵ model fails to predict flow near walls due to its imposed wall function. Standard k-ω predicts near-wall flow better but fails in transition to core flow. And SST k-ω model combines the first two models for enhanced accuracy in near-wall and core flow. The author also points out that standard k-ϵ has a better convergence rate and is widely used in the industry [Gülich, 2010].

Shah et. al. also give a review about the state-of-the-art CFD methods to assess centrifugal pumps and recommends "two-equation k-ϵ models" as "appropriate" for pump analysis [Shah et al., 2013]. Jafarzade et. al. investigated a low specific speed high-speed centrifugal pump with k-ϵ, RNG k-ϵ and RSM turbulence models and concluded that every model gave similar results while the latter two resulted in a better agreement with the test result. Nevertheless, they also point out the computational loads on processors and stated that the standard k-ϵ model gave a faster convergence where no modification on the computational scheme is pursued [Jafarzadeh et al., 2011]. For this thesis, a standard k-ϵ model is used although k-ω and SST models are also run for checking the solution.

For k-ϵ model, the term μ_{eff} term in equation 6.2 includes the effects of the molecular viscosity and turbulent viscosity of the fluid.

$$\mu_{eff} = \mu + \mu_{\mathrm{t}} \tag{6.4}$$

Turbulent viscosity is obtained from the turbulent length scale(L_{t}) and turbulent velocity scale (V_{t}).

$$\mu_{\mathrm{t}} = \rho c_{\mu} L_{\mathrm{t}} V_{\mathrm{t}} \tag{6.5}$$

where V_{t} is the square root of the turbulent kinetic energy k.

$$V_{\mathrm{t}} = \sqrt{\mathrm{k}} \tag{6.6}$$

Turbulent dissipation rate ϵ on the other hand is expressed in terms of turbulent kinetic energy and turbulent length scale.

$$\epsilon = \frac{\mathrm{k}^{3/2}}{L_\mathrm{t}} \tag{6.7}$$

Combining equation 6.5, 6.6 and 6.7, turbulent viscosity can be written in the following form.

$$\mu_\mathrm{t} = C_\mu \rho \frac{\mathrm{k}^2}{\epsilon} \tag{6.8}$$

where $C_\mu = 0.09$.

Values of k and epsilon are calculated from transport equations below.

$$\frac{D\mathrm{k}}{Dt} = \frac{\partial}{\partial x_j}\left(\frac{\mu_\mathrm{t}}{\rho\sigma_\mathrm{k}}\frac{\partial \mathrm{k}}{\partial x_j}\right) + \frac{\mu_\mathrm{t}}{\rho}\frac{\partial \overline{u_i}}{x_j}\left(\frac{\partial \overline{u_i}}{x_j} + \frac{\partial \overline{u_j}}{x_i}\right) - \epsilon \tag{6.9}$$

$$\frac{D\epsilon}{Dt} = \frac{\partial}{\partial x_j}\left(\frac{\mu_\mathrm{t}}{\rho\sigma_\epsilon}\frac{\partial \epsilon}{\partial x_j}\right) + C_1\frac{\mu_\mathrm{t}}{\rho}\frac{\epsilon}{\mathrm{k}}\frac{\partial \overline{u_i}}{x_j}\left(\frac{\partial \overline{u_i}}{x_j} + \frac{\partial \overline{u_j}}{x_i}\right) - C_2\frac{\epsilon^2}{\mathrm{k}} \tag{6.10}$$

where $C_1 = 1.44$, $C_2 = 1.92$, $\sigma_\mathrm{k} = 1$ and $\sigma_\epsilon = 1.3$ [White, 2006].

6.3.2 Boundary Conditions

CFD model is set up in CFX-Pre software. To avoid any error during the case setup, operational parameters such as rotation speed and mass flow rate are introduced as user expressions.

The reference frames of fluid domains are established. Rotating domains' reference frame was given a rotating feature with user-defined speed expression. Then for each domain boundaries are specified.

For inlet boundary conditions, an absolute 0 bar of total pressure is given. In real life, this would introduce cavitation immediately but since the CFD model is an incompressible single-phase model, pressures below zero do not make any physical meaning and by this method, pressure contours can be read and required NPSH is determined easily.

For the outlet boundary, a mass flow rate condition is imposed with the user-defined expression.

Remaining mesh boundaries are classified as either walls with imposed roughness and moving velocity or mesh interface surfaces to connect rotating and non-rotating domains. For mesh interface, a frozen rotor option is chosen.

6.3.3 Solver Parameters

Solver parameters are also determined in the CFX-Pre software. Convergence criteria of 300 maximum iterations and 10^{-5} RMS residual condition is chosen. The timescale of the solver is configured as a physical timescale with the time scale value of $1/\omega$.

6.4 CFD Results

Prepared CFD case is run until the convergence criteria are met. To find the optimum mesh size for computational efficiency, a mesh dependency analysis is conducted.

In CFD-Post the solution is examined and some of the solution details evaluated are presented in Figure 6.7 and 6.8.

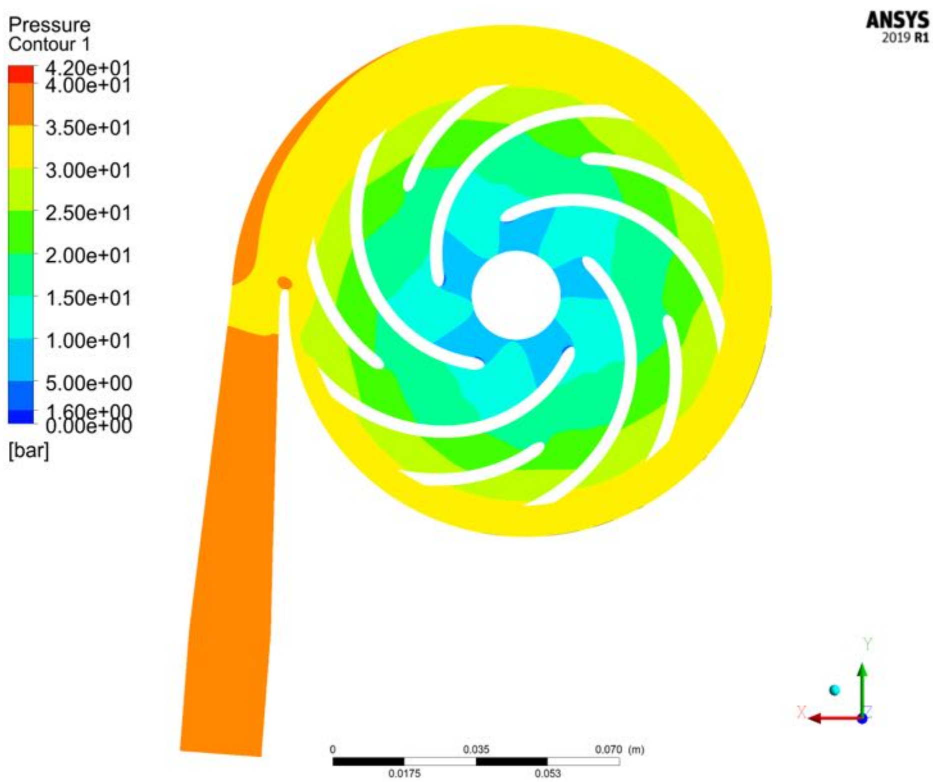

Figure 6.7: Static pressure Contour at 0.5 span.

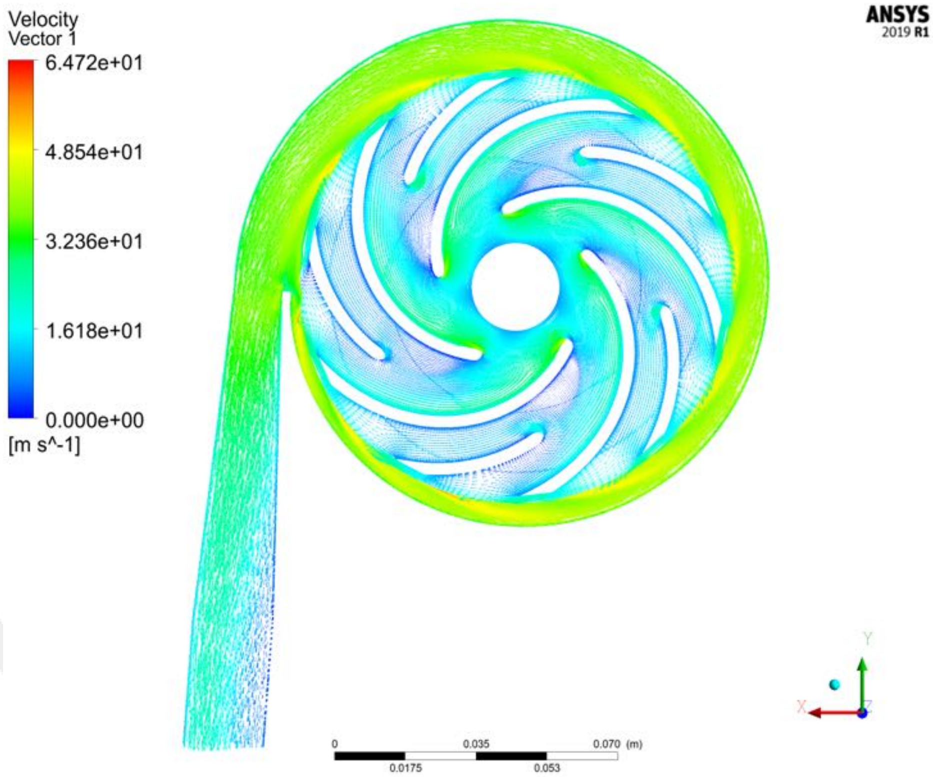

Figure 6.8: Velocity vector field at 0.5 span.

When Figure 6.7 is zoomed towards the blade tips, the minimum pressure area can be identified as a very thin and small layer as shown in Figure 6.9. This area of the blade where pressure is below the saturation pressure which is 1.6 bar absolute for LOX at 95 K, would not contribute to any cavitation shedding and head loss. Also, evaporation of liquid molecules takes energy from the surroundings and lowers the temperature, this drops the vapor pressure towards the non-cavitating region. This phenomenon is called "thermodynamic suppression head" and is more effective on cryogenic fluids as stated by Gulich [Gülich, 2010].

Engineering values such as head and efficiency are calculated by evaluating pressures ın Inlet and Outlet for head and, by evaluating torque exerted on rotating walls.

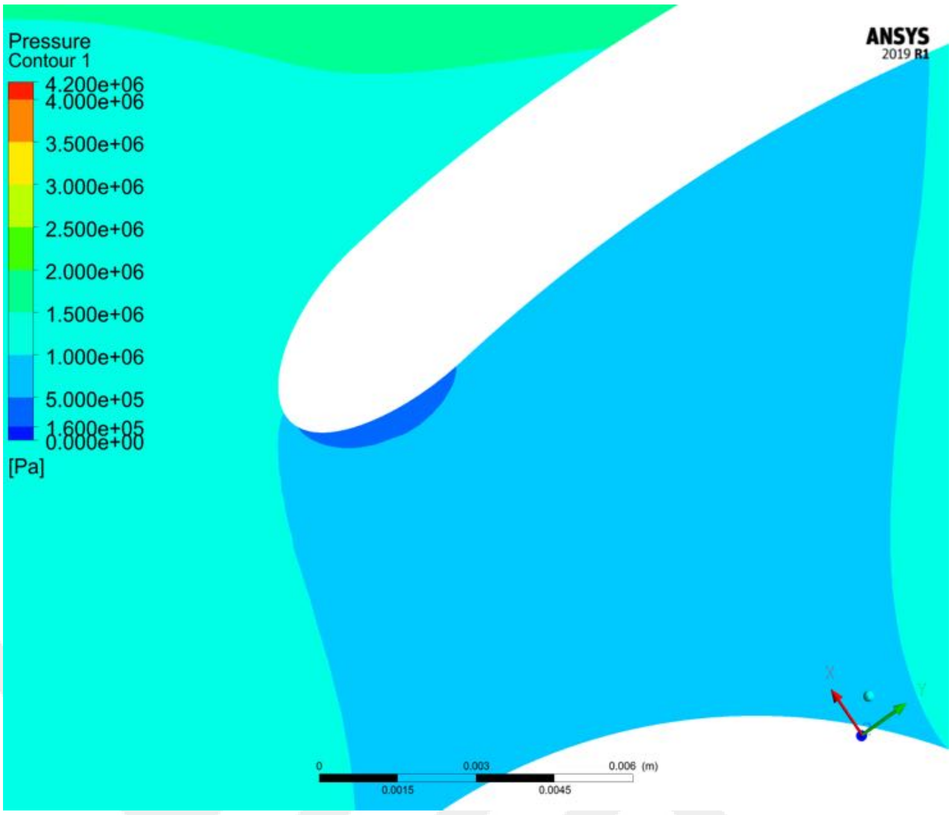

Figure 6.9: Static pressure distribution at blade inlet tip.

6.5 Model Validation

The CFD model used should be validated with a system that has known performance data or experimental data. Since a reliable source where both design and experimental data could not be found, an industrial LOX transfer pump is procured and tested to build a self-validation case.

6.5.1 Pump Specifications

The pump is rated for flowrates from 2 lt/s to 10 lt/s with a differential head between about 140 m to 190 m. The head-capacity curve obtained from the manufacturer is presented in Figure 6.10.

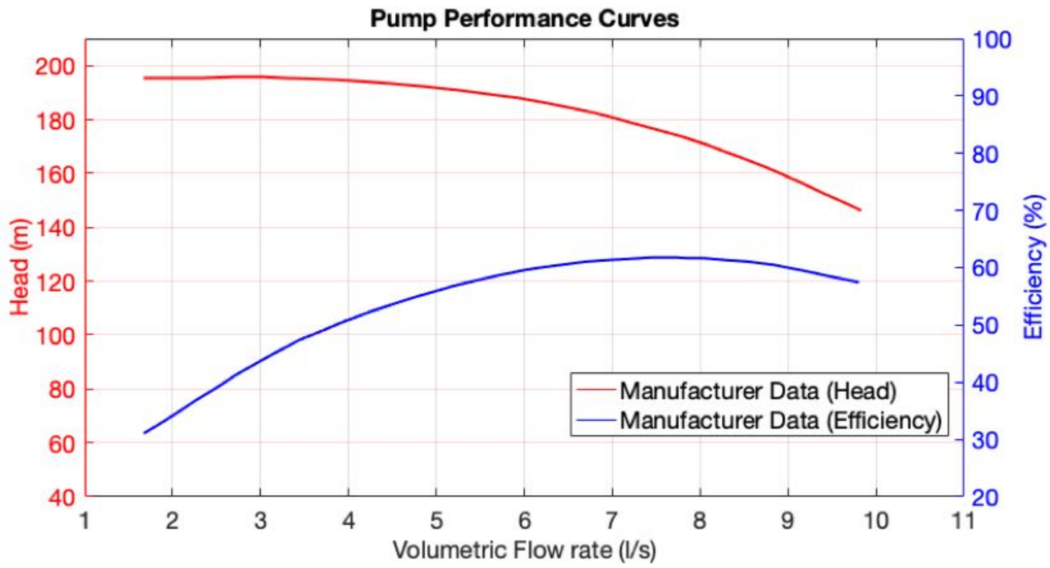

Figure 6.10: Q-H curve of procured pump.

6.5.2 Geometry Generation

Before testing the pump is disassembled to create a geometric model to be used for CFD validation. Components' dimensions are retrieved by means of non-destructive techniques and assembled again. Blade details could not be retrieved completely but with a visual confirmation, a model with high conformity to real part is generated. For propriety reasons, the hydraulic components' geometric details will not be revealed.

6.5.3 Mesh Generation

The geometry modeled in a CAD environment is the solid model of the pump. For fluid domains, the model should be inverted where the voids would become solids and solids would become voids. This is again done in CAD environment where the solid models of components are subtracted from an envelope solid.

To simplify the model to gain computational time, the geometry is cleared in SpaceClaim from details such as labyrinth seals and impeller balance holes. The geometry is transferred into ANSYS Meshing and an unstructured linear mesh algorithm is chosen with mesh option selected for CFX.

Surfaces on the geometry are named with "Named Selection" command to be used detailed mesh options and further for CFX case setup. For the entire domain,

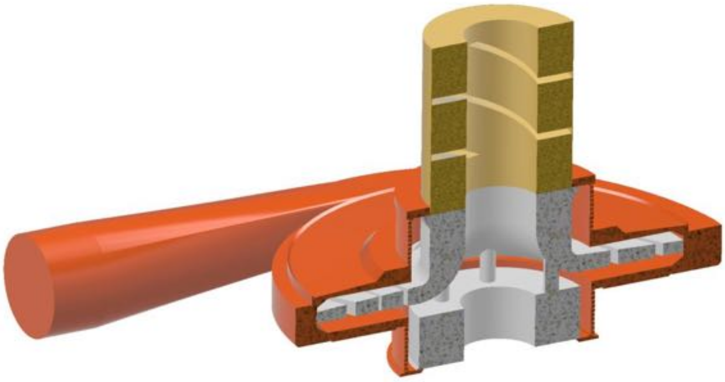

Figure 6.11: Fluid domains of the pump.

a boundary layer inflation is given from all the surfaces into the mesh. A first layer thickness of 0.05 mm is given with a growth rate of 1.2 for 8 layers.

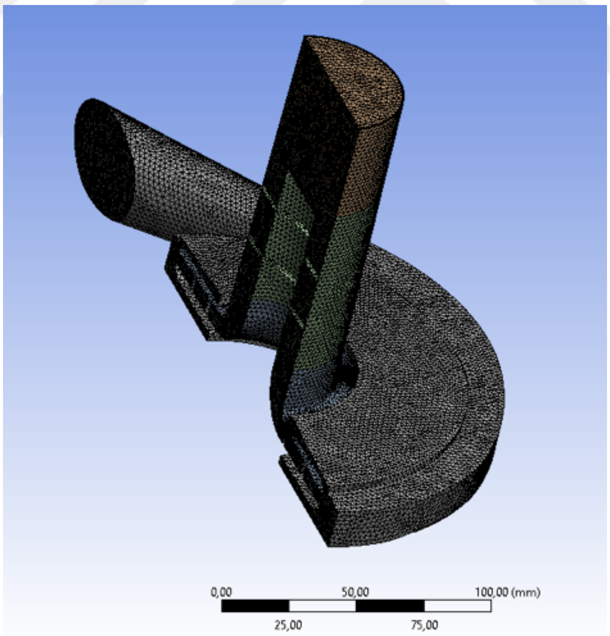

Figure 6.12: Fluid domain mesh of the validation model.

6.5.4 CFD Analysis

CFD case to be validated is configured according to the procedure explained earlier in this chapter. Before presenting the results, first, a mesh dependency analysis is made.

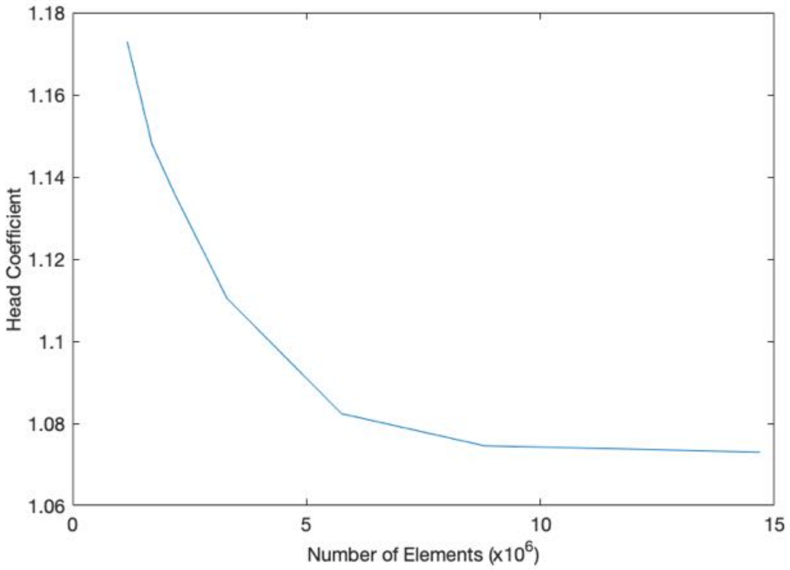

Figure 6.13: Mesh dependency of validation case.

As can be seen in Figure 6.13, the result varies negligibly after 5.7 millions of elements. So the number of elements is chosen to be 5.7 million and with this mesh, a set of CFD runs has been executed with varying flow rates. Also to compare the fidelity of turbulence models, each analysis also is done with k-ω , SST and RNG k-ϵ turbulence models. In Figure 6.14, head values for all turbulence models fit the

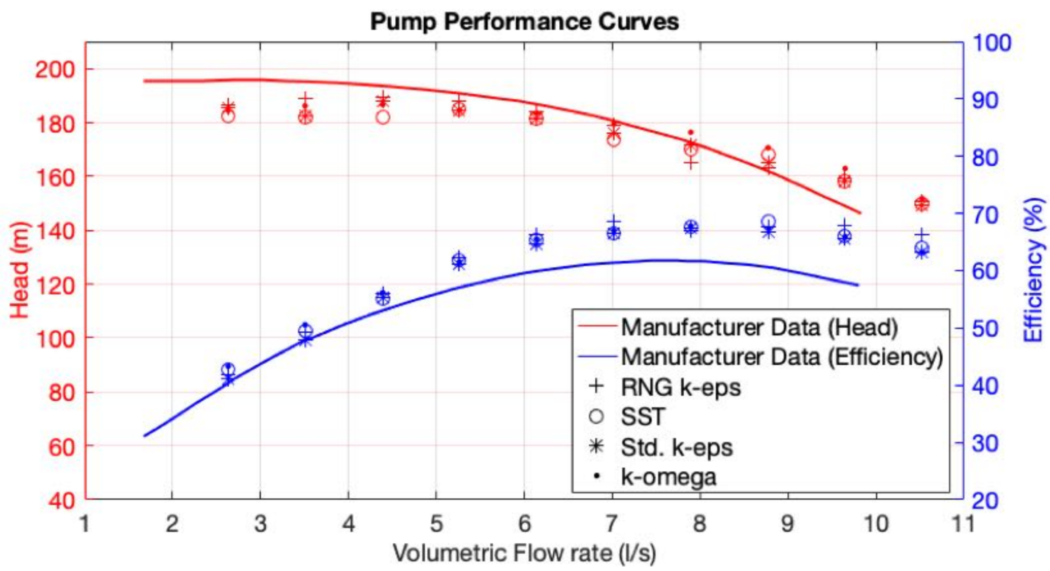

Figure 6.14: CFD results compared to manufacturer data.

manufacturer data around the best efficiency point. There is negligible difference between turbulence models and all models give acceptable predictions when compared to the pump data. CFD model under-predicts in low part-load region and over-predicts head in high flow region. Efficiencies are over-predicted in all cases but this is expected since CFD models do not include mechanical losses such as bearings and secondary flow losses.

6.5.5 Pump Testing

Test Facility

To test the pump and gather physical data to validate CFD model, a test facility capable of supplying LOX at the desired flow rate for the required time is developed. The flowrate, pressure and temperature measurements would also be needed to be acquired synchronously and accurately.

LOX flow tests for the pump are executed in DeltaV's test facility. The facility has a 1m3 aerogel insulated LOX run tank with a feed line going to the test cell. Pressure and temperature measurements are taken at a number of places on the tank and feed line. The flow rate is measured with both coriolis mass flowmeter and a turbine flowmeter. A resemblance of the PID diagram of the test facility is illustraten in Figure 6.15. Complete PID is omitted due to confidentiality.

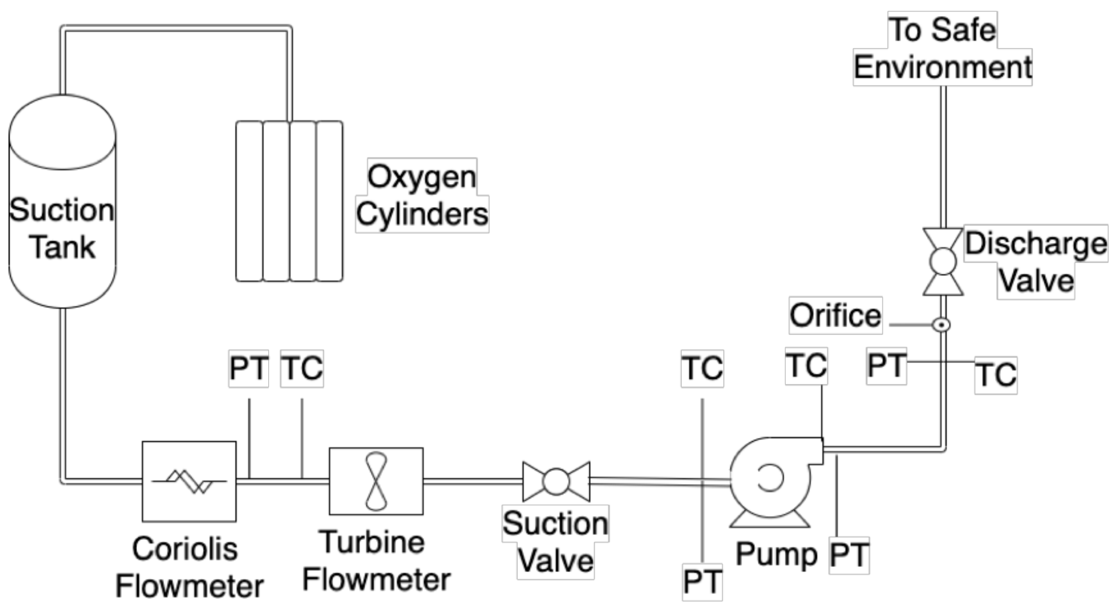

Figure 6.15: Schematic of the pump test facility, PT = Pressure Transmitter, TC = Thermocouple.

Valves on the process line are controlled by a control system that is designed and implemented by DeltaV engineers. The system is capable of controlling every valve from the control room and can execute a test sequence with a configurable setting.

A pump skid is designed and manufactured for the the pump test bench (See Figure 6.16). The skid has mounting holes for the motor of the pump and mounting supports for suction and discharge lines. The lines immediately before and after the pump are flexible hoses that would comply in case of thermal shrinkage of the rigid pipeline due to cryogenic exposure.

Figure 6.16: Pump test bench, PT = Pressure Transmitter, TC = Thermocouple.

Upstream of the suction flex line, there is a conical wire mesh filter (See 6.17) placed between the flanges to protect components from solid unwanted particles that could lead to a fire inside the pump. The wire mesh is initially procured with stainless steel mesh but later it is decided that a brass mesh would be safer due to the oxidation resistance of the material.

Pumps are usually tested on a closed cycle where the fluid is discharged to the same tank as the suction tank through restriction device. In the test facility, re-

Figure 6.17: Conical brass wire mesh filter.

turning fluid to the run tank was costly, inconvenient and risky because of possible contamination of LOX in the pump. For these reasons, fluid is decided to be discharged to the atmosphere. At the discharge side of the pump, flow is restricted by an orifice and a manual cryogenic ball valve is placed for further flow control when needed and sealing the discharge lines from the exterior. These components can be seen in Figure 6.16

The pump is driven by an AC induction motor that is controlled by an inverter. The inverter unit is equipped with on-panel buttons to preset speeds and start the motor. These speeds and other run parameters are entered into the device. The inverter is capable of providing 2 channels of analog output where a number of inverter parameters are measured and recorded by the DAQ system. For the purpose of these tests, one channel is configured to indicate output frequency while the other is programmed to provide power output data.

National Instruments DAQ systems are used in the test facility. One chassis employing different kinds of DAQ modules measure sensor output signals in 4-20 mA current or 0-10V voltage ranges. Temperature measurements are made by T type thermocouples. Shaft rpm sensor is a laser sensor working with a reflective tape attached to the rotating surface. Reflective tape is attached to the pump shaft in the first but due to the condensation on the surface at cryogenic temperatures (See Figure 6.19) , no measurement could be taken during the test. At the later tests, protecting enclosure of the motor fan is removed and rpm is measured from the fan of the motor (See Figure 6.18). The measured speed is later multiplied with a gear ratio of the gearbox increasing the pump shaft speed.

Figure 6.18: RPM Sensor placement on cooling fan.

Conducting Tests

Tests are designed to obtain a map for the pump consisting of head and efficiency data at different flow rates and different pump speeds. 3 speed settings are determined to be tested in each test.

The first test was not successful due to the two-phase flow occurred in the pump because of insufficient NPSH. Feedline was much longer than it would be at a regular pump test setup due to increased safety requirements of rocket motor test setups and LOX heated up more than expected as a result and reached saturation point before entering the pump. In the later tests, the run tank is pressurized to 9-10 bar level to guarantee liquid phase flowing into the pump.

Prior to the test, the run tank is filled with LOX and the facility is prepared. With one tank, three speed settings are tested for one orifice size. Then orifice is changed, the tank is filled and test is carried again.

Figure 6.19: Condensation during cryogenic testing.

Data Reduction and Analysis

The recorded test data are loaded to the MATLAB. Data are plotted against time and the operation durations are determined. Data for pressures and the flow rate is plotted in Figure 6.20, temperature data is plotted in Figure 6.21, drive system data is plotted in Figure 6.22.

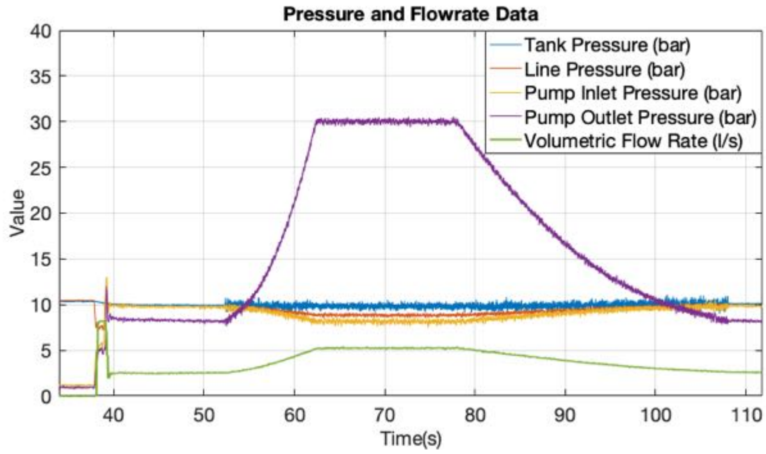

Figure 6.20: Test pressure & flow rate data.

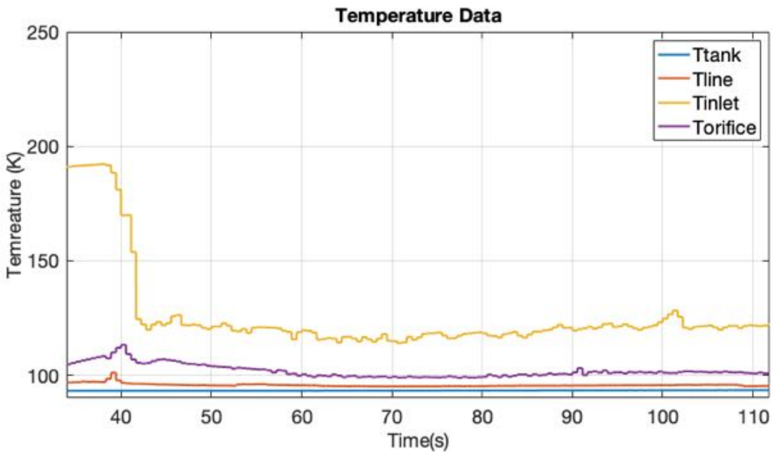

Figure 6.21: Test temperature data.

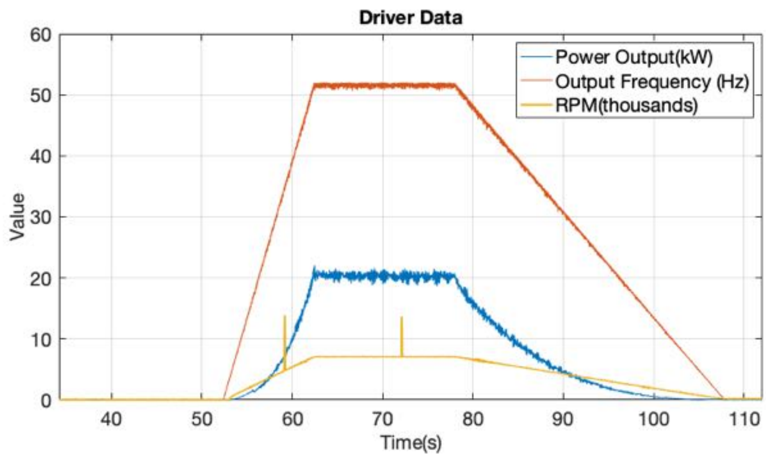

Figure 6.22: Test pump drive data.

Measurements taken at the duration of steady operation are used to calculate test points to determine performance parameters as well as to provide similar conditions to the CFD model. These data points are presented in Table 6.1.

Density determined from the temperature is used to calculate pump parameters such as head and efficiency. Hydraulic power is calculated with two approaches. First is by using the pressure difference and the density of the fluid, classical approach.

$$\dot{W}_h = P_h = Q\Delta p \tag{6.11}$$

Second is a thermodynamic approach that uses the thermodynamic properties of the fluid to calculate energy input to the fluid. Power transferred to liquid can be found by enthalpy difference.

$$P_{h,s} = \dot{m}(h_2 - h_1) \tag{6.12}$$

The process in the pump is assumed isentropic and adiabatic since the residence time in pump is quite small. The enthaply and entropy value at the outlet is found by using the measured pressure and temperature. Then by using the same entropy value and the pressure measured at the inlet, enthalpy value is found. The thermodynamic properties of LOX are taken from the NIST database[1].

$$s_1 = s_2 \tag{6.13}$$

$$h_{1s} = f(p_1, s_1) \tag{6.14}$$

Then the efficiency is calculated by using this enthalpy value.

$$P_{h,s} = \dot{m}(h_2 - h_{1s}) \tag{6.15}$$

With hydraulic work calculated with both methods, efficiency is found by dividing them to shaft power measured from the driver.

$$\eta_h = \frac{P_h}{P_{motor}}, \eta_{h,s} = \frac{P_{h,s}}{P_{motor}} \tag{6.16}$$

Shaft power is determined from the driver output power and efficiency of the motor. The efficiency value is read from the nameplate of the motor as 0.906.

[1] From https://webbook.nist.gov/cgi/cbook.cgi?Name=o2Units=SI

Table 6.1: Test results.

Test #	Speed(rpm)	Q (l/s)	H (m)	η_h(%)	$\eta_{h,s}$ (%)
2	6570	1.9	176.46	38.5	39.8
3	6840	1.98	188.12	38.2	38.8
4a	7100	2.03	202.37	37.2	40.8
4b	6840	2.01	188.03	39.6	37.1
4c	7100	2.04	202.01	37.6	40.3
4d	6840	1.98	187.47	39.8	39.0
5	6840	5.1	185.30	58.2	60.8
6	7100	5.25	198.72	56.9	56.7
7	6570	4.95	170.04	59.4	58.4

6.5.6 Validation Results

Averaged conditions at the test data points are entered to the CFD model and results are presented in Table 6.2. Efficiency calculated with the classical method is included in this table since the efficiency is calculated with the same procedure in CFD.

Deviations from the test data are in line with the curve prediction made earlier in Figure 6.14, under-predicting the Head, and overestimating but converging efficiency at low part load. For a comparison, Test data points and Q-H curves obtained from CFD are plotted at Figure 6.23. It should also be noted that the CFD analysis did not take internal leakages into account so a part of the error is likely caused from this effect as well.

Table 6.2: Comparison of test and CFD values.

Case #	Speed (rpm)	Q (l/s)	H_{CFD} (m)	$\eta_{h,CFD}$	H_{Test} (m)	$\eta_{h,Test}$	err_H (%)	err_η (%)
2	6570	1.9	162.83	35.9	176.46	38.5	-7.7	-6.8
3	6840	1.98	176.53	35.9	188.12	38.2	-6.2	-6.1
4a	7100	2.0	191.59	35.8	202.37	37.2	-5.3	-3.8
4b	6840	2.01	176.86	35.9	188.03	39.6	-5.9	-9.3
4c	7100	2.04	189.93	35.7	202.01	37.6	-6.0	-4.9
4d	6840	1.98	176.51	35.9	187.47	39.8	-5.8	-9.8
5	6840	5.1	178.22	59.3	185.3	58.2	-3.8	+1.8
6	7100	5.25	192.34	59.0	198.72	56.9	-3.2	+3.7
7	6570	4.95	164.10	59.6	170.04	59.4	-3.5	+0.3

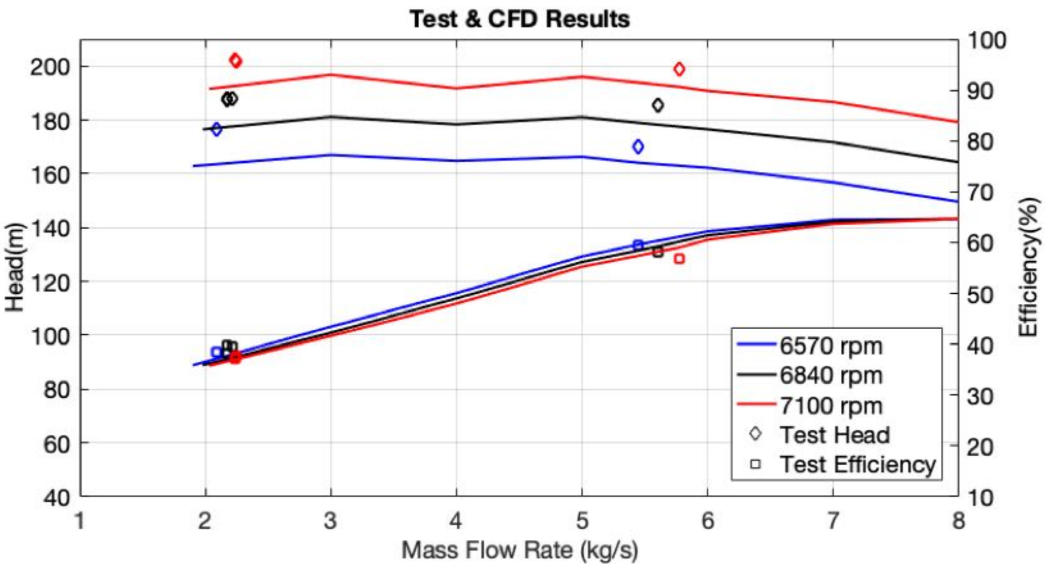

Figure 6.23: Test data points plotted on Q-H curve obtained from CFD.

At this point, a confidence level has been reached for the accuracy of CFD predictions. Getting the same error trend in low part load is a strong indicator for predicting performance on design point with acceptable accuracy.

Chapter 7

SYSTEMS COMPARISON AND RESULTS

System component mass for both systems is gathered together in Table 7.1.

Table 7.1: Propulsion system specifications.

Parameter	Symbol	Press-Fed	Electric Pump-Fed
Total Propellant Mass,kg	M_{prop}	335.19	335.19
Useful Propellant Mass,kg	$M_{prop,useful}$	315.19	315.19
Combustion Chamber Mass,kg	M_{ch}	61.69	61.69
Nozzle Mass,kg	M_{nozzle}	34.5	34.5
Pressurization System Mass,kg	$M_{sys,press}$	69.68	26.25
Oxidizer Tank Mass,kg	M_{oxtank}	50.05	13.97
Pump System Mass,kg	$M_{sys,pump}$	0	17.42
Propulsion System Wet Mass,kg	M_{tot}	551.12	489.01
Propulsion System Dry Mass,kg	M_{dry}	213.14	153.06
Structural Mass Fraction	M_{dry}/M_{tot}	0.386	0.313
Payload Mass,kg	M_{pay}	50	50
Initial Stage Mass,kg	$M_{stage,i}$	601.12	543.37
Stage Mass at burn out,kg	$M_{stage,f}$	285.92	223.82

Electric pump employed system has around 21.7 % less mass at burnout. Using the stage initial mass and burnout mass, ΔV values of systems are calculated with equation 7.1.

$$\Delta V = I_{sp,del} g_0 ln \left(\frac{M_{stage,i}}{M_{stage,f}} \right) \tag{7.1}$$

$$\Delta V_{pressfed} = 2,357 \ m/s, \qquad \Delta V_{pumpfed} = 2,788 \ m/s \tag{7.2}$$

And also for constant ΔV missions, a payload capability of systems are compared in Table 7.2

Table 7.2: Payload capability comparison.

ΔV	M_{pay} for pressure-fed	M_{pay} for electric pump-fed
1,000 m/s	614.71 kg	676.80 kg
1,500 m/s	285.49 kg	347.59 kg
2,000 m/s	122.92 kg	185.01 kg

As proposed in the first chapters of this thesis, performance improvements are evident in the analysis results. For definite ΔV missions there is 10.1 %, 21.75 % and 50.52 % increase in payload capability in missions with ΔV of 1000 m/s, 1500 m/s and 2000 m/s respectively. This result shows that using electric pumps for high performance(high ΔV) missions has a significant advantage over pressure-fed systems.

Chapter 8

CONCLUSION AND FINAL REMARKS

In line with the objective of this thesis, the advantage of using an electric pump on an upper stage hybrid rocket is established. First, previous studies related to this subject and the state-of-the-art is discussed. Different approaches to electric pump concepts are presented and the lack of practical application of electric pumps on hybrid rockets is emphasized.

To practically apply the concept onto the target propulsion system, pump hydraulic concepts and existing design methodologies for pumps are explained. The propulsion system and subsystems design, along with pump drive system design methods are presented with stated assumptions.

With the given design methodologies, two propulsion systems are designed, one with an electric pump and the other with a pressure-fed mechanism, and mass estimations of each component are presented. Any component or subsystems other than the pressurization system and tanks are kept identical to isolate the comparison to the area of focus. The disparate component comparison already reveals the direction of the analysis in favor of the electric pump system.

A pump for a particular application is designed and modeled for CFD analysis to verify its performance. The CFD analysis method is further validated by testing an actual pump. CFD and Test results are compared and a tendency to under-predict the head at low part load is observed. It is contemplated that the CFD method is accurate near the best efficiency point because the CFD results fit the manufacturer data, although a measurement around this point could not be obtained. This will be done later if it is thought to be necessary.

By mechanical design of the pump, the mass estimation error is reduced and a comparison between the candidate systems became possible with higher fidelity. The results of this comparison show a clear advantage of an electric pump in hybrid rocket applications when investigated on a system-level analysis. It should also be noted that adding an inducer to reduce NPSH and designing an impeller with a higher head would further reduce the pressurization system mass and improve the comparative advantage of the proposed system.

The author recognizes that a more detailed CFD survey should be done in order to accurately predict transient events and cavitation performance in flow passages. Initial multi-phase analysis is being made but omitted from this thesis along with transient analysis as they are not in the scope of what has been tried to achieve.

The prototype whose geometric detail is shown in Figure 5.3 will be manufactured and will be tested with LOX. At the end of the development phase, the prototype will be integrated into the upper stage motor and tested on a rocket hot fire test.

The scope of this thesis did not cover the detailed design of the pump drive system and its components. This area stays as a critical one as the electric pump powered flight depends on the readiness level of these electrical and electronic components. For an upper stage system, all electrical components needs to operate in vacuum and solar radiation environment. Therefore, thermal management of batteries and electric motor stay as a critical area of study and will be investigated separately.

As the conclusion of this thesis, the electric pump approach for upper stage hybrid rockets is proven to be a promising strategy for developing small satellite launchers in a simpler and faster manner. And future advancements in electrical components will challenge existing approaches of higher thrust systems in development time and cost.

BIBLIOGRAPHY

[Casalino et al., 2019] Casalino, L., Masseni, F., and Pastrone, D. (2019). Viability of an electrically driven pump-fed hybrid rocket for small launcher upper stages. *Aerospace*, 6:36.

[Casalino and Pastrone, 2010] Casalino, L. and Pastrone, D. (2010). Optimization of a hybrid rocket upper stage with electric pump feed system. In *46th AIAA/ASME/SAE/ASEE Joint Propulsion Conference & Exhibit*.

[Dlugiewicz et al., 2012] Dlugiewicz, L., Kolowrotkiewicz, J., Szelag, W., and Slusarek, B. (2012). Permanent magnet synchronous motor to drive propellant pump. In *International Symposium on Power Electronics, Electrical Drives, Automation and Motion*, pages 822–826.

[Duffy, 2015] Duffy, K. P. (2015). Electric motors for non-cryogenic hybrid electric propulsion. In *51st AIAA/SAE/ASEE Joint Propulsion Conference*.

[Gegeoglu et al., 2019] Gegeoglu, K., Kahraman, M., Ucler, C., and Karabeyoglu, A. (2019). Assessment of using electric pumps on hybrid rockets. In *AIAA Propulsion and Energy 2019 Forum*.

[Gegeoglu et al., 2018] Gegeoglu, K., Kara, O., and Karabeyoglu, A. (2018). Systems advantages of electric pump fed upper stage hybrid rocket. In *International Astronautical Congress 2018 Proceedings*.

[Gülich, 2010] Gülich, J. F. (2010). *Centrifugal Pumps*. Springer Berlin Heidelberg.

[Guo et al., 2018] Guo, C., Huang, S., Wang, J., and Feng, Y. (2018). Research of cryogenic permanent magnet synchronous motor for submerged liquefied natural gas pump. *IEEE Transactions on Energy Conversion*, 33(4):2030–2039.

[Jafarzadeh et al., 2011] Jafarzadeh, B., Hajari, A., Alishahi, M. M., and Akbari, M. H. (2011). The flow simulation of a low-specific-speed high-speed centrifugal pump. *Applied Mathematical Modelling*, 35:242–249.

[Johnsson and Bigert, 1990] Johnsson, G. and Bigert, M. (1990). Development of small centrifugal pumps for an electric propellant pump system. *Acta Astronautica*, 21(6):429 – 438.

[Karabeyoglu et al., 2007] Karabeyoglu, A., Cantwell, B., and Zilliac, G. (2007). Development of scalable space–time averaged regression rate expressions for hybrid rockets. *Journal of Propulsion and Power*, 23:737–747.

[Karabeyoglu et al., 2002] Karabeyoglu, A., D., A., and B., C. (2002). Combustion of liquefying hybrid propellants: Part 1, general theory. *Journal of Propulsion and Power*, 18(3):610–620.

[Karabeyoglu et al., 2004] Karabeyoglu, A., Zilliac, G., Cantwell, B., Zilwa, S. D., and Castellucci, P. (2004). Scale-up tests of high regression rate liquefying hybrid rocket fuels. *Journal of Propulsion and Power*, 20(6):1037–1045.

[Karassik, 1976] Karassik, I. (1976). *Pump Handbook*. Mechanical engineering. McGraw-Hill.

[Kwak et al., 2018] Kwak, H. D., Kwon, S., and Choi, C.-H. (2018). Performance assessment of electrically driven pump-fed lox/kerosene cycle rocket engine: Comparison with gas generator cycle. *Aerospace Science and Technology*, 77:67–82.

[Liping Zheng et al., 2005] Liping Zheng, Wu, T. X., Acharya, D., Sundaram, K. B., Vaidya, J., Limei Zhao, Lei Zhou, Ham, C. H., Arakere, N., Kapat, J., and Chow, L. (2005). Design of a superhigh-speed cryogenic permanent magnet synchronous motor. *IEEE Transactions on Magnetics*, 41(10):3823–3825.

[Rachov et al., 2013] Rachov, P. A., Tacca, H., and Lentini, D. (2013). Electric feed systems for liquid-propellant rockets. *Journal of Propulsion and Power*, 29(5):1171–1180.

[Shah et al., 2013] Shah, S., Jain, S., Patel, R., and Lakhera, V. (2013). Cfd for centrifugal pumps: A review of the state-of-the-art. *Procedia Engineering*, 51:715 – 720.

[Solda and Lentini, 2008] Solda, N. and Lentini, D. (2008). Opportunities for a liquid rocket feed system based on electric pumps. *Journal of Propulsion and Power*, 24(6):1340–1346.

[Stepanoff, 1957] Stepanoff, A. J. (1957). *Centrifugal and Axial Flow Pumps: Theory, Design, and Application.* Krieger Publishing Company.

[Sutton and Biblarz, 2010] Sutton, G. P. and Biblarz, O. (2010). *Rocket Propulsion Elements.* John Wiley & Sons.

[Waxenegger-Wilfing et al., 2018] Waxenegger-Wilfing, G., dos Santos Hahn, R. H., and Deeken, J. (2018). Studies on electric pump-fed liquid rocket engines for micro-launcher. In *Space Propulsion Conference.*

[White, 2006] White, F. (2006). *Viscous Fluid Flow.* College Ie. McGraw-Hill.

[Wiesner, 1967] Wiesner, F. (1967). A review of slip factors for centrifugal impellers. *Journal of Engineering for Gas Turbines and Power*, 89(4):558–566.

[Williams and Curry, 1992] Williams, S. D. and Curry, D. M. (1992). *Thermal protection materials: Thermophysical property data.* NASA Reference Publication 1289.